Hyaluronan composite bioink preserves nucleus pulposus cell phenotype in a stiffness-dependent manner

Gregor Miklosic, Stéphanie de Oliveira, Maja Schlittler, Catherine Le Visage, Christophe Hélary, Stephen J Ferguson, Matteo d'Este

▶ **To cite this version:**

Gregor Miklosic, Stéphanie de Oliveira, Maja Schlittler, Catherine Le Visage, Christophe Hélary, et al.. Hyaluronan composite bioink preserves nucleus pulposus cell phenotype in a stiffness-dependent manner. Carbohydrate Polymers, 2025, 353, pp.123277. 10.1016/j.carbpol.2025.123277 . hal-04933586

HAL Id: hal-04933586
https://hal.science/hal-04933586v1

Submitted on 6 Feb 2025

HAL is a multi-disciplinary open access archive for the deposit and dissemination of scientific research documents, whether they are published or not. The documents may come from teaching and research institutions in France or abroad, or from public or private research centers.

L'archive ouverte pluridisciplinaire **HAL**, est destinée au dépôt et à la diffusion de documents scientifiques de niveau recherche, publiés ou non, émanant des établissements d'enseignement et de recherche français ou étrangers, des laboratoires publics ou privés.

Distributed under a Creative Commons Attribution 4.0 International License

Hyaluronan composite bioink preserves nucleus pulposus cell phenotype in a stiffness-dependent manner

Gregor Miklosic [a b], Stéphanie De Oliveira [c], Maja Schlittler [a], Catherine Le Visage [d], Christophe Hélary [c], Stephen J. Ferguson [b], Matteo D'Este [a *]

[a] AO Research Institute Davos, 7270 Davos, Switzerland

[b] Institute for Biomechanics, ETH Zürich, 8092 Zürich, Switzerland

[c] Laboratory of Condensed Matter Chemistry of Paris, Sorbonne University, 75005 Paris, France

[d] Nantes Université, Oniris, INSERM, Regenerative Medicine and Skeleton, RMeS, UMR 1229, F-44000 Nantes, France

* Corresponding author: matteo.deste@aofoundation.org

Abstract

Intervertebral disc degeneration is a major cause of neck and back pain, representing a significant global socioeconomic burden. The polysaccharide hyaluronan is key to maintaining disc physiology and mediating disc disease through its structural and biological roles in the nucleus pulposus, a component of the intervertebral disc highly susceptible to degeneration. In this study, we introduce a novel composite bioink designed for extrusion bioprinting of structures resembling the nucleus pulposus. Our bioink combines levels of hyaluronic acid and collagen that approach physiological concentrations and effectively mimics the disc's hydrated and mechanically resilient environment. We modulated the composite's mechanical properties through the tyramination of hyaluronic acid and subsequent photocrosslinking, influencing morphology and gene expression of embedded bovine nucleus pulposus cells. This allows us to replicate a range of properties from healthy to degenerated human nucleus pulposus, which would be challenging to achieve with traditional cell culture and in vivo models. Our results show that modulating hyaluronan physico-chemical properties influenced embedded cell phenotype. The outcomes of this study inform the future design of biomaterials for the modeling of disc disease and regeneration, and present a versatile platform that can be readily integrated with other biofabricated components to form engineered intervertebral disc-like structures.

Keywords: intervertebral disc, nucleus pulposus, bioprinting, in vitro models, hyaluronic acid

1. Introduction

Intervertebral disc (IVD) degeneration is the most common contributor to neck and back pain (DePalma et al., 2011), which are leading causes of disability worldwide and represent a substantial socioeconomic burden (Hartvigsen et al., 2018; Vos et al., 2012). Our understanding of its complex pathophysiology remains limited despite extensive research, primarily because of reliance on animal tissue and simplistic cell culture models (Mainardi et al., 2022; Wang et al., 2022). This limitation is reflected in the traditional treatments, which escalate rapidly from pain management to invasive surgeries – such as discectomies, spinal fusions, and synthetic replacements – yet often fail to restore the spine's full range of functionality (Romaniyanto et al., 2022).

Central to the IVD's function is the nucleus pulposus (NP), a hyaluronic acid (HA)-rich gel-like yet multiphasic core confined within an elastic annulus fibrosus ring that plays a crucial role in the spine's ability to transfer loads and maintain flexibility (Iatridis et al., 1996). NP's unique properties are derived from its composition: collagen type II and large quantities of proteoglycans, predominantly aggrecan. Aggrecan, associated with HA, forms negatively charged complexes essential for maintaining the NP's hydration and resilience against compressive forces (Singh et al., 2009). Although the exact sequence of events is yet to be fully elucidated, it is clear that disc degeneration alters this mechanical function through compositional changes brought about by a combination of factors: cell senescence and reduced regenerative potential (Le Maitre et al., 2007; Zhao et al., 2007), build-up of waste products and reduced nutrient transport (Roberts et al., 1996; Shirazi-Adl et al., 2010), and an imbalance between the production and degradation of the extracellular matrix (ECM) (Pattappa et al., 2012; Singh et al., 2009; Sztrolovics et al., 1997). These factors ultimately result in a reduction of the NP's swelling capacity and a loss of the IVD's structural integrity. The compromised structure further exacerbates the problem, leading to tissue injury, vascularization, innervation, infiltration by immune cells, inflammation, and a rapid progression of tissue breakdown (Freemont et al., 1997; Le Maitre et al., 2005; Phillips et al., 2013; Vergroesen et al., 2015). This complex interplay of biology and mechanics in the disc degeneration process illustrates the importance of studying both in parallel.

Current models of IVD degeneration have significant limitations. Animal models, essential due to the scarcity of human IVD tissue, capture the full intricacy of developed native structures. However, despite their critical role in advancing our understanding of disc degeneration, they are inherently limited due to the biomechanical and biochemical differences from humans. For instance, animal tissue is adapted for loads that are unrepresentative of the bipedal human anatomy (Alini et al., 2008). Furthermore, the absence of notochordal cells in adult humans, which are present in several animal species, represents a fundamental discrepancy in the IVD's regenerative potential (Erwin et al., 2006; Pattappa et al., 2012; Poletto et al., 2023; Wang et al., 2022). In contrast to animal models, traditional cell culture systems do not mimic the IVD's compositional, structural, and mechanical complexity. Whether in 2D or 3D matrices, they lack the full range of the body's mechanical cues (Lazaro-Pacheco et al., 2023). Such cues play a vital role in maintaining IVD homeostasis (Gawri et al., 2014; Paul et al., 2012; Wuertz et al., 2009) and as potential triggers of degeneration (Setton & Chen, 2004; Wuertz et al., 2009). For example, IVD cell morphology and proteoglycan production are highly sensitive to the multi-axial movements in the body and stiffness variations in the disc structure (Hsieh & Twomey, 2010; Setton & Chen, 2004). In the nucleus pulposus and annulus fibrosus, shear stiffness can vary between 5-60 kPa and 100-400 kPa respectively, depending on the severity of degeneration (Iatridis et al., 1997, 1999). Although organ-on-a-chip systems have attempted to replicate dynamic tissue aspects like nutrient transport and mechanical loads (Mainardi et al., 2022), they have focused on discrete aspects of cell-cell and cell-material

interactions, far from the scale and complexity of a whole organ. Therefore, a precise and comprehensive in vitro representation of the native IVD environment remains a distant goal.

The limitations of existing IVD models underscore the need for tissue-engineered alternatives. Such constructs should aim to more closely replicate the native IVD structure, while also leveraging the benefits of a bottom-up approach. These benefits include utilizing clinically relevant human cell sources and offering the flexibility to tailor the model to specific research inquiries, such as studying different stages of disc degeneration. By processing and chemically modifying ECM components, we can employ various biofabrication techniques, like printing and electrospinning, to accurately mimic both the structure and composition of the IVD (Schmitz et al., 2020; Vernengo et al., 2020). However, recent engineering efforts have primarily concentrated on regenerative applications, thereby overlooking this aspect of biomimicry. This led to using materials that fall short of faithfully replicating the ECM's biochemical signals and mechanical properties (Gloria et al., 2020; Gullbrand et al., 2018; Liu et al., 2022; Marshall et al., 2021; Yang et al., 2018). Addressing these shortcomings in a novel biomaterial would enable the development of more accurate and functional in vitro IVD models.

To address this gap, we introduce a polysaccharide-based biomaterial designed to create in vitro structures that mimic the NP. We leverage the native ECM components HA and collagen at their natural concentrations (approximately 18-36 mg/mL and 15-20 mg/mL, respectively) (Iatridis et al., 1996; Martins et al., 2018; Singh et al., 2009), replicating the NP's hydrated environment with the negatively charged HA and providing biochemical cues suitable for preserving the NP cell phenotype. HA's versatility as a substrate for chemical modification allows us to tune its properties through a photocrosslinking process. We demonstrate that minor adjustments in composition can alter the final stiffness across the entire spectrum from healthy to degenerated human NP and investigate how these changes influence cell behavior. We showcase our composite's compatibility with 3D bioprinting approaches, which confers it with advantages over hydrogels designed for simpler casting approaches: it enables a more streamlined future integration with biofabricated annulus fibrosus structures and facilitates reproduction of the radial gradation in composition and stiffness, as the NP transitions into the annulus. We achieve this printability by incorporating sacrificial gelatin microgels, which modulate the rheological properties of the bioink independently of the crosslinking parameters and dissolve out of the produced hydrogel constructs under standard cell culture conditions at 37 °C due to the inherent thermoresponsive properties of gelatin (Ouyang et al., 2022; Soliman et al., 2023). In summary, our composite is a flexible addition to the biomaterials repertoire, enabling the development of biomimetic IVD models and facilitating future advances in disc degeneration research.

2. Materials and methods

2.1. Materials

Sodium hyaluronate from biotechnological origin (*Streptococcus equi*), with a molecular weight 150-350 kDa (SEC-MALS) and ≥90.0% purity, was purchased from Contipro a.s. Collagen was isolated in-house from Wistar rat tails. Type A gelatin from porcine skin with 300 g Bloom was purchased from Sigma-Aldrich (70-90% protein by Biuret test). All other reagents were obtained from various commercial suppliers (see individual section) and used as purchased without further purification.

2.2. Functionalization of hyaluronic acid with tyramine

The amidation of HA (Nutrihyl, Contipro, MW: 150-350 kDa) with tyramine (Tyr) was conducted using 4-(4,6-dimethoxy-1,3,5-triazin-2-yl)-4-methylmorpholinium chloride (DMTMM, >95.0% purity, TCI) as

a coupling agent. Initially, HA sodium salt was dissolved in ultrapure water (Milli-Q, EMD Millipore) at 1% w/v and then heated to 37 °C. DMTMM was added to a final concentration of 25 mM and allowed to dissolve completely. Subsequently, Tyr HCl (Roth, ≥98%), pre-dissolved at 1 M in ultrapure water, was introduced dropwise until a 25 mM concentration was reached. The reaction was maintained at 37 °C with continuous stirring for 24 h. Next, saturated NaCl (Roth, ≥99.0%) was added to a final concentration of 13.5% v/v, before the solution was cooled down to room temperature. HA-Tyr precipitation was triggered by adding 3 volumes of 96% ethanol (Alcosuisse, A15, ≥99.8% stock) dropwise. The precipitate was further washed under vacuum in a Gooch filter crucible (grade 2, DURAN), with gradually increasing concentrations of ethanol (80% to 99.8%). An argentometric test with silver nitrate (Sigma-Aldrich, ≥99.5%) confirmed the absence of chlorides. The product was first dried in a fume hood for 24 h, followed by vacuum drying at room temperature for an additional 24 h and at 40 °C for 48 h. The degree of functionalization was measured spectroscopically by absorbance at 275 nm (Infinite M Plex, TECAN) and compared to Tyr HCl standards (Darr & Calabro, 2009). HA-Tyr with 6.2% degree of substitution was used in all experiments.

2.3. Isolation and purification of collagen

Type I collagen was extracted from the tails of young male Wistar rats. The tails were cleaned and rinsed with 70% ethanol before dissection within a biosafety cabinet. The dissection involved gradually cutting the tails from the tip in 1 cm segments to extract tendons, which were then washed with PBS (Sigma-Aldrich) and dissolved in 50 mL of 0.5 M acetic acid (Carlo Erba) per tail for 24 h under gentle stirring. Following dissolution, the collagen solution was centrifuged for 15 min at 3,000 g to remove debris and purified by precipitation through the dropwise addition of 4 M NaCl until a final concentration of 0.7 M. The precipitate was redissolved in fresh 0.5 M acetic acid at half the initial volume and dialyzed against 17 mM acetic acid to remove salts and adjust the pH to 4.5. The collagen solution was centrifuged at 30,000 g for 4 h at 10 °C to remove any remaining aggregates, and the supernatant was stored at 4 °C. The collagen concentration was quantified using hydroxyproline titration, and its purity was confirmed by SDS-PAGE electrophoresis (Mini-PROTEAN TGX, Bio-Rad). Finally, the collagen solution was concentrated to 40 mg/mL by slow evaporation within the biosafety cabinet.

2.4. Fragmentation of collagen

40 mg/mL stock solution of collagen type I in 17 mM acetic acid was neutralized by the addition of 4.9% v/v 1 M NaOH (Roth, ≥97.0%) and 11.7% v/v 10X PBS to achieve a final concentration of 1X PBS and 34.3 mg/mL collagen. This solution was transferred into 1 mL syringes (Omnifix, B. Braun) and incubated at 37 °C for 30 min to form a stiff collagen hydrogel. The hydrogel was fragmented by repeated extrusion, initially once without any needle attached, followed by three successive extrusions through blunt-tip needles of sizes 20G, 25G, and 30G (Optimum, Nordson), respectively.

2.5. Preparation of gelatin microgels

Gelatin microgel preparation was adapted from literature, based on the method introduced by Hinton for FRESH 3D printing (Hinton et al., 2015; Ouyang et al., 2022). Gelatin (300 g Bloom, type A, 70-90%, Sigma-Aldrich) was dissolved in ultrapure water at a concentration of 4% w/v by stirring at 50 °C. An equal volume of ethanol was added, followed by the addition of Pluronic F-127 (Sigma-Aldrich) and gum Arabic (Thermo Scientific) at concentrations of 0.25% w/v and 0.1% w/v, respectively, relative to the total volume. Upon complete dissolution, the mixture was cooled to room temperature under constant stirring at 400 rpm for 16 h. The resulting microgel suspension was centrifuged at 300 g for 5 min, and the supernatant was discarded. The microgels were washed and centrifuged three times with PBS. After

washing, the microgels were supplemented with 5 volumes of 99.8% ethanol while stirring at 400 rpm. The suspension was filtered and washed with additional ethanol using a qualitative filter paper (grade 1, Whatman) under vacuum to yield a dry powder. This powder was placed in an oven for further drying under vacuum at room temperature for 24 h and subsequently stored at 4 °C for future use. To characterize the produced microgels, they were rehydrated in PBS and imaged at 10x magnification using phase contrast microscopy (Axio Vert.A1, Zeiss). The microgel images were segmented using Cellpose 2.0 with the human-in-the-loop approach (Pachitariu & Stringer, 2022), and their Feret diameter was measured using ImageJ (National Institutes of Health).

2.6. Cell isolation and culture

NP cells were harvested from the tail discs of approximately one-year-old bovine males. The process began with thoroughly washing the tails, followed by removing surrounding soft tissue using a scalpel. NP tissue was extracted from the discs, starting from the largest intact disc and continuing until 5 to 10 discs were dissected, depending on the tail size. The collected tissue was rinsed in PBS containing 1% v/v penicillin/streptomycin (P/S, Gibco). The tissue was finely minced into approximately 2 mm^3 pieces under sterile conditions in a laminar flow cabinet. These were then placed into a spinner flask to initiate digestion, containing 0.2% w/v pronase (Roche) in Dulbecco's Modified Eagle Medium, with 4.5 g/L of glucose and 110 mg/mL sodium pyruvate (DMEM HG, Gibco), supplemented with 10% v/v fetal bovine serum (FBS, Corning) and 1% v/v P/S. After 1.5 h at 37 °C in a cell culture incubator, the pronase solution was discarded, and the tissue was washed three times with PBS. The digestion was continued with 200 U/mL of collagenase II (Worthington) in DMEM HG for another 14 h under stirring. The resulting cell suspension was sequentially filtered through 100 µm and 40 µm cell strainers (Falcon) to remove debris. Following filtration, the suspension was centrifuged, the supernatant was discarded, and the pellet was resuspended in fresh DMEM HG. The cells were then seeded at 5,000 cells/cm^2 for expansion. After reaching the desired confluency, the cells were frozen in liquid nitrogen and later utilized at passage 2 for encapsulation in hydrogels.

All hydrogel constructs were cultured in DMEM HG containing 10% v/v FBS and 1% v/v P/S. Cell cultures were maintained at 37 °C with a humidified atmosphere of 5% CO_2 and media was changed every third day.

2.7. Bioink formulation and hydrogel preparation

All dry bioink components were exposed to UV light for 2 h in a laminar flow cabinet to reduce contamination risk. All liquid components were filtered through a 0.45 µm sterile filter. Collagen fragmentation was performed in a laminar flow cabinet. The fragmented collagen was mixed with HA-Tyr and gelatin microgels to achieve final concentrations of 20 mg/mL collagen, 30 mg/mL HA-Tyr, and 50 mg/mL gelatin (**Figure 1**). PBS at 10X concentration was supplemented to achieve a final 1X concentration, accounting for the PBS added during collagen fragmentation. Stock solutions of sodium persulfate (SPS, Sigma-Aldrich, ≥98%) and tris(bipyridine)ruthenium(II) chloride (Ru, Combi-Blocks, 99%) were prepared in ultrapure water and incorporated into the bioink at 5% v/v each, resulting in final concentrations of 0.1 mM Ru and variable SPS concentrations of 1, 2, or 4 mM, depending on the desired hydrogel stiffness. The concentrations were determined in a preliminary rheological experiment to cover a range from healthy to moderately degenerated human nucleus pulposus. Cells were thawed, expanded, detached, and resuspended in pure FBS at a concentration of 50 x 10^6 cells/mL for encapsulation. This cell suspension was added to the bioink to achieve final concentrations of 5 x 10^6 cells/mL and 10% v/v FBS. The final volume of the bioink was adjusted with ultrapure water as needed. Hydrogels were formed by extruding the bioink into a silicone mold (Sylgard 184, Dow) featuring cylindrical wells, each 5 mm in

diameter and 1.3 mm in height. To ensure consistency in the amount of shear cells were exposed to, conditions were kept constant for all experiments, using a 22G tapered tip (Optimum, Nordson) and 50 kPa of pressure. HA-Tyr crosslinking was initiated through exposure from both the top and bottom of the mold to a 450 nm LED light source (SST-10-B, Luminus) at an intensity of 5 mW/cm^2 for 3 min.

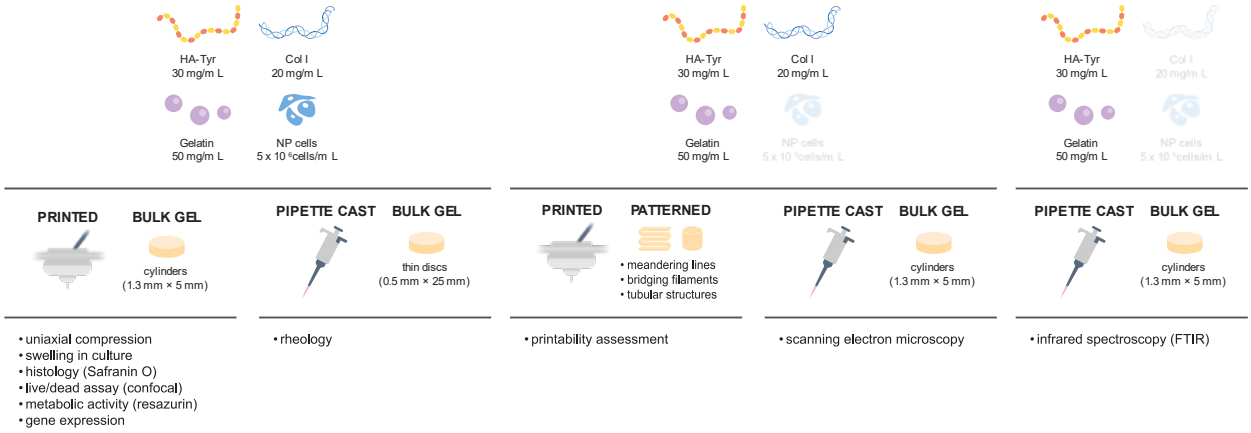

Figure 1. Overview of compositions and sample geometries. Combinations of tyramine-functionalized hyaluronic acid (HA-Tyr), collagen type I (Col I), and gelatin were tested both with and without encapsulated nucleus pulposus (NP) cells. The composites were either shaped into bulk gels, through extrusion with a 3D bioprinter or casting with a pipette, or patterned with a 3D bioprinter to assess printability.

2.8. Rheological testing

The evaluation of the bioink's viscoelastic properties was conducted using both shear oscillatory and rotational rheology (MCR 302, Anton Paar). The rheometer was equipped with a Peltier temperature control system, a parallel plate geometry with a glass lower plate, and a 450 nm LED light source (SST-10-B, Luminus). All experiments were carried out at 25 °C and a gap size of 0.5 mm. Oscillatory tests were performed using a fixed frequency of 1 Hz. An amplitude sweep between 0.1 and 100% shear strain was used to identify the linear viscoelastic region of the bioink. The limit of the linear viscoelastic region was determined as a 10% deviation from the initial plateau value. The flow point of the material, defined as the transition where the loss modulus exceeds the storage modulus, was determined. The bioink's elastic recovery was assessed by alternating between low strain within the linear viscoelastic region (0.1%) and high flow-inducing strain (100%). Mean storage moduli of the first and last low-strain cycles were compared as a measure of material deformation after repeated shearing. The bioink's viscosity was measured rotationally by altering the shear rate between 0.1 and 100 s^{-1}. Measured values were fit according to the Ostwald–de Waele relationship as $\eta = K\dot{\gamma}^{n-1}$, where η represents the viscosity, K the flow consistency index, $\dot{\gamma}$ the shear rate, and n the flow behavior index. The effect of light on gelation was examined in compositions with varying SPS concentrations of 1, 2, or 4 mM, exposing samples to 5 mW/cm^2 of blue light for 3 min at a constant shear strain of 0.1% to assess the tunability of shear stiffness.

2.9. Compression testing

Hydrogel samples were incubated in DMEM HG at 37 °C for 24 h. After incubation, the dimensions of the swollen samples were measured using digital calipers (HeliosPreisser). Uniaxial compression tests were performed on an electrodynamic testing system (LTM1, ZwickRoell) equipped with a 50 N load cell

(U9C, HBM). The testing protocol consisted of an initial 0.01 N preload, followed by a stepwise stress-relaxation test, wherein the samples were compressed in increments of 5% strain, up to a maximum of 25% strain, at a rate of 5%/s. A relaxation period of 15 min was allowed at each strain increment. Data acquisition was performed at a sampling rate of 10 Hz. The stress relaxation data, obtained at each strain level, were fit to a power law model (Cloyd et al., 2007) as $\sigma = A\ \exp(\beta\epsilon - 1)$, where σ and ϵ represent the stress and strain, respectively, while A and β are material-specific constants. The linear region equilibrium modulus, indicative of the material's stiffness, was subsequently calculated from the fitted model as the derivative of stress with respect to strain at 10% compression. Stress relaxation at each strain level was calculated as a proportion of the relaxed stress to the peak stress of the corresponding strain.

2.10. Scanning electron microscopy

Cell-free hydrogel samples were fixed in a 4% v/v solution of glutaraldehyde (Electron Microscopy Sciences) at 4 °C for 24 h. Following fixation, they were washed three times in a buffer of 0.05 M sodium cacodylate (Sigma-Aldrich) and 0.3 M sucrose (Sigma-Aldrich), adjusted to a pH of 7.4. After washing, the samples were dehydrated through a series of ethanol baths, starting from 50% and increasing incrementally to 100%, to ensure gradual removal of water. After dehydration, the samples were processed using a supercritical CO_2 dryer (EM CPD300, Leica). For morphological analysis, the dried samples were fractured to reveal their cross-sections. The fractured samples were mounted onto specimen holders and sputter-coated with 15 nm of gold. Observations were carried out using a scanning electron microscope (S-3400N, Hitachi) operating at 10 kV.

2.11. Fourier transform infrared spectroscopy (FTIR)

Hydrogels prepared using HA-Tyr and gelatin microgels were analyzed using attenuated total reflectance-Fourier transform infrared spectroscopy (ATR-FTIR) to determine compositional changes in response to gelatin's thermosensitive properties. Samples were prepared at three different degrees of crosslinking by varying the SPS concentration (either 1, 2, or 4 mM) according to the steps outlined in section 2.7, omitting collagen and cells to avoid confounding sample spectra. After crosslinking, the hydrogels were incubated in PBS (pH 7.4) at 37 °C for either 0, 1, 3, or 7 days. This was followed by an overnight freezing at -20 °C and subsequent freeze-drying. The dry polymer sponges were analyzed on a FT/IR 4X (Jasco) spectrometer. Transmittance spectra were recorded between 4000 and 400 cm^{-1} with a resolution of 4 cm^{-1} and 32 scans. The atmospheric background was subtracted, baseline corrected, and a 5-point moving average smoothing performed. The spectra for each sodium persulfate/timepoint combination were averaged and normalized to the 1035 cm^{-1} peak, which was attributed to the glycosidic linkages in the backbone of the hyaluronic acid (Nikonenko et al., 2000).

2.12. Printability

Printability was evaluated on a pneumatic extrusion bioprinter (3DDiscovery, REGENHU). Bioinks were loaded into a 3 mL opaque black barrel (Optimum, Nordson), fitted with a 22G tapered tip (SmoothFlow, Nordson) and a standard piston (White SmoothFlow, Nordson). The printing was performed at room temperature, with an extrusion pressure of 50 kPa.

A series of simple patterns were extruded to evaluate the bioink printability quantitatively. The structures were crosslinked at each extruded layer by 5 s of exposure to blue light at an intensity of 5 mW/cm^2.

Filament uniformity was first determined by extruding a single filament of length 20 mm on an etched glass slide. The pattern was immediately imaged using a camera and later analyzed using ImageJ. The diameter of the filament was measured at three equally spaced points.

To assess filament fusion, a continuous meandering pattern with gradually decreasing line spacing was printed (Ribeiro et al., 2017). The closest two lines (1 mm) were used to determine the fused segment length (L_F). This fused segment is observed at the transition from one line to the other, where the printing direction is changed, and propagates from the corners as a function of surface tension and yield stress (Schwab et al., 2020).

Next, a 10 mm by 10 mm square with a 3 x 3 grid was produced. The geometry of the internal macropores was evaluated by measuring their perimeter (L) and area (A). A printability index (C. O'Connell et al., 2020) was determined as $P = L^2/16A$ with $P = 1$ indicating perfectly square macropores, $P < 1$ overly circular macropores, and $P > 1$ an irregular macropore shape.

To evaluate the bioink's capability of bridging gaps, single filaments were extruded across a steel pillar array with increasing gap distances of 2, 4, and 8 mm (Ribeiro et al., 2017). The filaments were assessed by the amount of sagging at each of the three gap sizes by measuring their deflection angle (θ) from the start of the gap to its middle, relative to the printing surface. Minimizing such sagging is crucial in preserving vertical macroporosity.

Finally, a qualitative evaluation of the bioink's potential for 3D multi-layered structure fabrication was performed by producing simple cylindrical structures.

2.13. Cell viability

The viability of bovine nucleus pulposus cells encapsulated in hydrogels was assessed using confocal microscopy. Samples were imaged after printing and at subsequent time points up to 28 days of culture. At each time point, samples were removed from the culture medium and washed for 20 min in serum-free DMEM LG (low glucose, PAN-Biotech) supplemented with 20 mM HEPES buffer (Gibco). Next, the samples were immersed in a fresh solution of DMEM supplemented with 4 µg/mL each of calcein-AM (Invitrogen) and ethidium homodimer-1 (Sigma-Aldrich) to stain the live and dead cells, and 8 µg/mL Hoechst 33342 (Sigma-Aldrich) to stain the nuclei of the cells. This staining was followed by another washing step. The washing and staining procedures were performed on a microplate shaker at 350 rpm and 37 °C. Following the second washing, the samples were imaged using a confocal microscope (LSM 800, Zeiss). Z-stacks with a thickness of 200 µm were acquired at three representative regions of each sample using a 10x/0.45 objective (Plan-Apochromat, Zeiss).

2.14. Cell metabolic activity

The metabolic activity of bovine nucleus pulposus cells encapsulated in hydrogels was quantified using the CellTiter-Blue assay (Promega). Metabolic activity was measured after printing and at subsequent time points up to 28 days of culture. At each time point, the samples were transferred into a solution comprised of fresh culture medium and CellTiter-Blue reagent in a 5:1 ratio. The samples were incubated for 4 h at 37 °C on a shaker set to 350 rpm. After incubation, 100 µl aliquots of the culture medium were analyzed in duplicates using a microplate reader (Infinite M Plex, TECAN). Fluorescence was measured using an excitation wavelength of 560 nm and an emission wavelength of 590 nm. Cell-free hydrogels with identical composition and crosslinking density served as blanks. The gain value was established based on the signal obtained on day 0 and used across all subsequent time points.

2.15. Safranin-O/Fast Green staining

Samples were collected at days 0 and 28 of cell culture. They were removed from the medium and immediately placed into a 4% formaldehyde solution for 16 h at room temperature. This was followed by

immersion in 15% and 30% sucrose solutions for 3 h each, which was determined as sufficient for the samples to sink. After equilibration in the sucrose solution, the samples were embedded in Tissue Freezing Medium (Leica Biosystems) and snap-frozen in isopentane, cooled to approximately -160 °C with liquid nitrogen.

Next, the samples were cut into 10 µm sections using a cryostat (CryoStar NX70, Thermo Fisher Scientific). The Tissue Freezing Medium was removed, and the sections were rehydrated by rinsing in distilled water for 10 min. The slides were first stained in Weigert's Iron Hematoxylin Solution (Sigma-Aldrich) for 10 min in the dark, rinsed in lukewarm tap water for 10 min, and then rinsed in distilled water for another 10 min.

The sections were then immersed in 0.02% Fast Green FCF (C.I. 42053, Sigma-Aldrich) for 6 min followed by a 1% acetic acid solution for 20 s, and finally in Safranin O (C.I. 50240, Sigma-Aldrich) for 12 min. The slides were differentiated first in 70% ethanol until the red color was visible and the black/blue colors faded (10 s to 6 min), and subsequently in 96% ethanol for 2-30 s. After dehydration in absolute ethanol (2 x 4 min), the slides were immersed in xylene (2 x 2 min) and mounted with a cover slip using Eukitt Quick-hardening mounting medium (Sigma-Aldrich). Brightfield images of the sections were acquired with an Axioscan 7 slide scanner using a 20x/0.8 objective (Zeiss).

2.16. Measure of swelling in culture

The swelling and degradation properties of hydrogels were measured with and without encapsulated bovine nucleus pulposus cells by varying the SPS concentration to achieve different degrees of crosslinking. Samples were tracked throughout a 28-day culture period. At each time point, samples were removed from the culture medium and gently wiped against a sterile glass slide to remove any excess liquid. Subsequently, their mass was measured on a laboratory scale (ME103T/00, Mettler Toledo) under sterile conditions, and they were imaged with a camera (ArduCam). Sample volumes were estimated using ImageJ measurements of height and diameter.

2.17. RNA isolation and RT-qPCR

The gene expression of bovine nucleus pulposus cells cultured in hydrogels with varying degrees of crosslinking was measured over a period of 28 days. Samples were collected at each time point by flash-freezing in liquid nitrogen and subsequently stored at -70 °C for further processing.

To isolate the RNA, the samples were transferred into TRI Reagent (MRC) at 4 °C while still frozen. For homogenization, a 6 mm stainless steel ball was added to each sample. Then, the samples were processed in a ball mill (MM 400, Retsch) at 30 Hz for 3 min. The supernatant was collected from the homogenate and mixed with 1-bromo-3-chloropropane (BCP, Thermo Scientific) to trigger phase separation. The aqueous phase was then collected and further purified using columns (RNeasy Mini, Qiagen) according to the manufacturer's recommendations. Final elution was performed with RNase-free water, and the RNA purity and concentration were evaluated using a spectrophotometer (NanoDrop One, Thermo Fisher). RNA integrity was assessed, yielding sample RIN values above 9.0 (Bioanalyzer, Agilent). RNA was stored at -70 °C for future use.

The isolated RNA was transcribed to complementary DNA (SuperScript VILO cDNA Synthesis Kit, Invitrogen) following the manufacturer's recommendations. Subsequently, the relative gene expression levels were determined using a real-time PCR system (QuantStudio 6 Pro, Applied Biosystems) with TaqMan probes (TaqMan Universal PCR Master Mix, Applied Biosystems). A geometric mean of

GAPDH and RPLP0 was used as an internal control for normalizing RNA levels. The complete sequences and catalog numbers of all primers and probes used are listed in **Table 1**.

Table 1. Bovine oligonucleotide primers and probes used for RT-qPCR. Primers and probes with sequences were custom-designed and produced by Microsynth; primers and probes with catalogue numbers were purchased from Applied Biosystems.

Gene	Type	Sequence/catalog number
COL1A2	Primer fw (5'-3')	TGC AGT AAC TTC GTG CCT AGC A
	Primer rev (5'-3')	CGC GTG GTC CTC TAT CTC CA
	Probe (5'FAM/3'TAMRA)	CAT GCC AAT CCT TAC AAG AGG CAA CTG C
COL2A1	Primer fw (5'-3')	AAG AAA CAC ATC TGG TTT GGA GAA A
	Primer rev (5'-3')	TGG GAG CCA GGT TGT CAT C
	Probe (5'FAM/3'TAMRA)	CAA CGG TGG CTT CCA CTT CAG CTA TGG
ACAN	Primer fw (5'-3')	CCA ACG AAA CCT ATG ACG TGT ACT
	Primer rev (5'-3')	GCA CTC GTT GGC TGC CTC
	Probe (5'FAM/3'TAMRA)	ATG TTG CAT AGA AGA CCT CGC CCT CCA T
FOXF1	Primer fw (5'-3')	TGC ACC AGA ACA GTC ACA ACA C
	Primer rev (5'-3')	GAC GAA CTC CTT TCG GTC ACA
	Probe (5'FAM/3'TAMRA)	CTG CAA GGC ATC CCG CGG TAT C
SOX9	Primer fw (5'-3')	AAC GCC GAG CTC AGC AAG
	Primer rev (5'-3')	ACG AAC GGC CGC TTC TC
	Probe (5'FAM/3'TAMRA)	TTC AGC AGT CTC CAG AGC TTG CCC A
CDH2	Assay on demand	Bt04298958_m1
GAPDH	Primer fw (5'-3')	GGC TGC TTT TAA TTC TGG CAA A
	Primer rev (5'-3')	AAT CAT ACT GGA ACA TGT AGA CCA TGT A
	Probe (5'FAM/3'TAMRA)	TGG ACA TCG TCG CCA TCA ATG ACC
RPLP0	Assay on demand	Bt03218086_m1

2.18. Statistical analysis

All measurements are presented as means of three replicates and standard deviation SD. The normal distribution of measured values was assessed using the Shapiro-Wilk test. Statistical comparison in the rheological test of elastic recovery was performed with a repeated measures t-test between sequential cycles, followed by a Bonferroni correction to account for multiple comparisons. Due to the small sample sizes and challenges in meeting the normality assumptions of parametric tests, the more robust Kruskal-Wallis test was used for comparisons between groups of different crosslinking densities. This was followed by Dunn's test with the Bonferroni correction for post-hoc paired comparisons. Notably, in analyzing the metabolic activity of embedded cells, the statistical comparison was first performed with timepoint as an independent factor, then separately with concentration. In-depth pairwise comparisons were not performed due to poor statistical power and the conservative nature of the utilized tests. This similarly applies to the gene expression and swelling experiments. All statistical analyses were performed in Python using the scipy (Virtanen et al., 2020) and statsmodels (Seabold & Perktold, 2010) libraries.

3. Results

3.1. Viscoelastic properties of the bioink

The HA/collagen/gelatin bioink was evaluated rheologically to determine its suitability for printing, and compared to gelatin-free compositions to evaluate gelatin microgels' effectiveness as a rheological enhancer. Before photocrosslinking, the cell-laden composition displayed elastic prevalence ($G' > G''$), with a storage modulus of approximately 800 Pa in all formulations. The modulus was reduced by almost an entire order of magnitude to approximately 90 Pa when gelatin was absent. These properties were consistent even in the absence of cells (data not shown). An amplitude sweep was performed to determine the limit of the linear viscoelastic region (**Figure 2a**), which was observed at a mean of 2.7% shear strain (SD = 0.3%), corresponding to a shear stress of only 26 Pa (SD = 3 Pa). Flow in the material occurred early at a low stress of only 74 Pa (SD = 7 Pa), corresponding to a shear strain of 11% (SD = 1%). These values were reduced considerably in the absence of gelatin, with a limit of the linear viscoelastic region at 1.3% (SD < 0.1%), corresponding to a shear stress of only 1 Pa (SD = 0.1 Pa), and a flow point at 7% (SD = 1%), with a shear stress of 4 Pa (SD = 0.7 Pa).

Next, the material's elastic recovery was evaluated. When subjected to high shear, the bioink displays a prevalence of loss over the storage modulus, indicative of good flow when pushed through the nozzle. Upon cessation of the shear stimulus, storage modulus prevalence over the loss modulus was re-established, which is indicative of shape retention after extrusion. However, under our experimental conditions, a drop in storage modulus was observed after high shear, with a change of 19% (SD = 3%) after three high shear cycles (**Figure 2b**). Most of this change occurred during the first cycle (15%, SD = 3%). All changes in storage moduli between sequential cycles were deemed statistically significant ($p < 0.020$). When gelatin microgels were removed from the composite, the samples could no longer recover elastically. With a decrease of 58% (SD = 1%) in the storage modulus, dropping it below the loss modulus, a predominantly liquid-like behavior was indicated even after shear was reduced.

In a rotational measurement of viscosity, the bioink demonstrated shear-thinning behavior (**Figure 2c**). After fitting the data to a power-law fluid model, a mean flow behavior index of 0.45 ($R^2 = 0.999$) was established. This was comparable in gelatin-free samples with an index of 0.47 ($R^2 = 0.986$).

Formulations with varying concentrations of sodium persulfate were exposed to blue light while undergoing a time sweep test. Starting from a mean storage modulus of 800 Pa (SD = 100 Pa), 3 min of light exposure resulted in a modulus increase to 7, 11, and 17 kPa (SD = 0.2, 0.3, and 0.6 kPa), respectively, for SPS concentrations of 1, 2, and 4 mM (**Figure 2d**). Only the difference between 1 mM and 4 mM SPS was deemed statistically significant ($p = 0.022$). However, there was a strong linear correlation between the SPS concentration and storage modulus ($R^2 = 0.990$, $p < 0.001$). All formulations showed a rapid increase in storage modulus immediately after light exposure, reaching half the final storage modulus within 43 s (SD = 5 s).

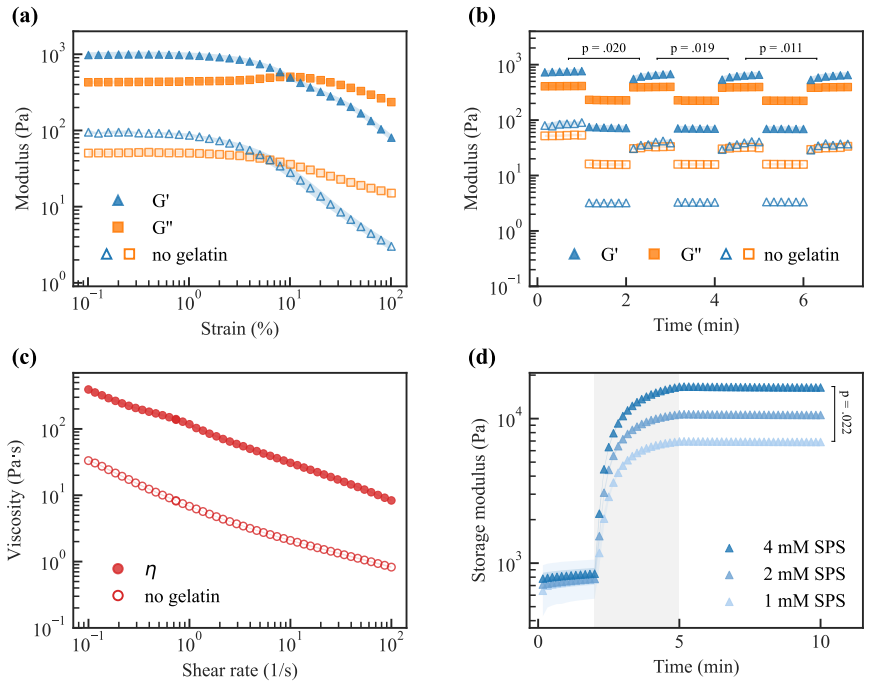

Figure 2. Rheological characterization of the NP bioink laden with 5 x 10^6 bovine NP cells/mL. Presented as means of three technical replicates, with bands indicating the standard deviation. Shear properties prior to crosslinking (a-c) were compared with gelatin-free controls. (a) An amplitude sweep from 0.1% to 100% shear strain reveals a short linear viscoelastic range and an early flow point, indicating that low shear stresses are required during printing. The presence of gelatin results in considerable higher storage and loss moduli. (b) Upon repeated cycling between low (0.1%) and high (100%) shear strain, the bioink exhibits a permanent drop in storage modulus. However, it flows under high shear and retains its elasticity when the shear is reduced. This elastic recovery is compromised in the absence of gelatin. Significant differences determined with repeated measures t-tests indicated. (c) The bioink's viscosity decreases with an increase in shear rate from 0.1 to 100 1/s, indicating shear-thinning behavior. Gelatin contributes to an overall higher viscosity in the composites. (d) The material's shear stiffness can be tuned through exposure to blue light (shaded area). By varying the concentration of sodium persulfate (SPS), moduli ranging from 7 to 17 kPa can be achieved. Significant difference determined with Dunn's test indicated.

3.2. Hydrogel compressive mechanics

Uniaxial compression was performed on hydrogels crosslinked to varying degrees of stiffness. The relaxation data fit well to a power law model, with R^2 of 0.992, 0.990, and 0.982 for the 1 mM, 2 mM, and 4 mM SPS formulations, respectively. The equilibrium moduli (i.e., determined after equilibration in stepwise compression) demonstrated a strong dependence on crosslinking density and were tunable between 4 kPa (SD = 1 kPa) for the softest hydrogels to 23 kPa (SD = 6 kPa) for the stiffest hydrogels (**Figure 3a**). The difference in moduli between 1 mM and 4 mM SPS were deemed significant ($p = 0.022$), with a moderately strong linear correlation between the concentration and equilibrium modulus ($R^2 = 0.838$, $p < 0.001$).

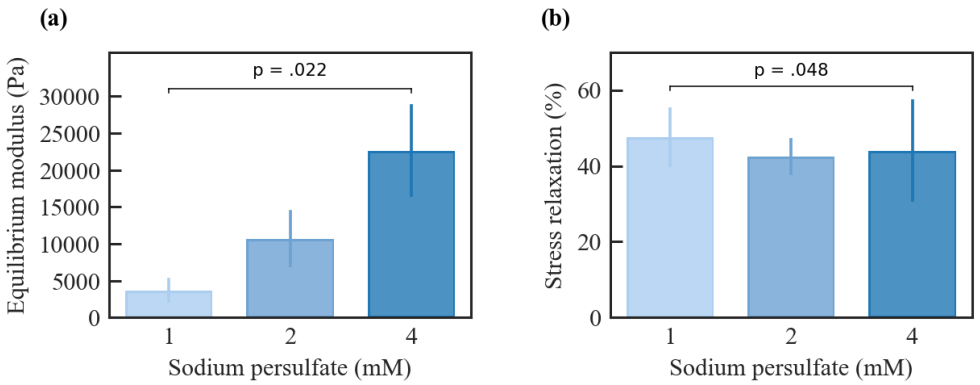

Figure 3. Uniaxial compression of hydrogels laden with 5 x 10^6 bovine NP cells/ml. Presented as means of three technical replicates, with error bars indicating the standard deviation. Significant differences determined with Dunn's test indicated. (a) The equilibrium modulus can be tuned between 4 and 23 kPa by varying the sodium persulfate concentration between 1 and 4 mM, as a result of modulating the crosslinking density. (b) Despite varying hydrogel stiffness, stress relaxation behavior remains consistent across all sodium persulfate concentrations, at approximately 40% relaxation from the peak.

Sample relaxation was consistent across strain levels and crosslinking densities, at more than 40% relaxation from peak stress after a 15 min relaxation period (**Figure 3b**). As with the modulus, a statistically significant difference was only observed between the extreme concentrations ($p = 0.048$), and there appeared to be no correlation between the concentration and degree of relaxation.

3.3. Morphology of the hydrogels

Using light and electron microscopy, we evaluated the morphological features of the hydrogels. Phase contrast imaging followed by software analysis of hydrated gelatin microgels revealed a Feret diameter distribution (**Figure 4a**) centered at 51 μm (SD = 7 μm).

Scanning electron microscopy of fractured hydrogels revealed morphological features of all three components, with an evident collagen fibril network scattered across sheet-like structures of HA-Tyr (**Figure 4b**). Additionally, gelatin microgels were embedded throughout the hydrogel (**Figure 4c**). The morphologies remained consistent across all crosslinking densities.

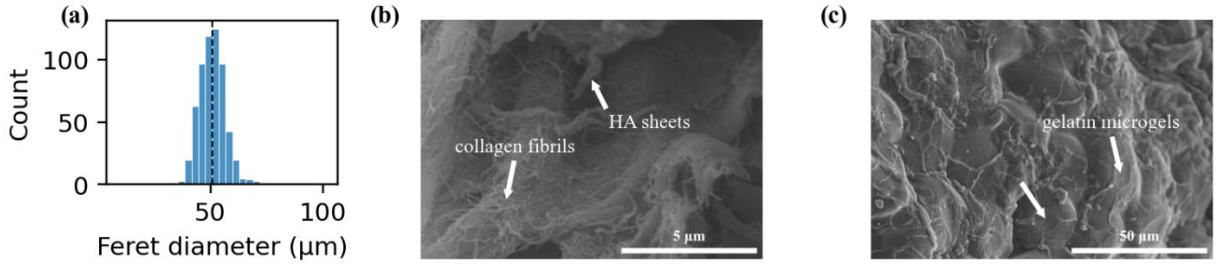

Figure 4. (a) Measurements of the gelatin microgel Feret diameter from phase-contrast microscopy images resulted in a distribution with a mean of 51 μm. A total of 610 representative microgels used for the measurement. (b-c) Representative scanning electron microscopy images of dried and fractured hydrogels prior to cell culture, reveal the presence of all three major morphological features: collagen fibril networks and HA-Tyr sheet-like structures in a 4 mM SPS sample (b), and gelatin microgels embedded in a 2 mM SPS sample (c). Scale bars represent 5 μm and 50 μm, respectively.

3.4. Compositional changes

We evaluated the change in HA-Tyr/gelatin microgel composites over the course of 7 days in PBS at 37 °C via ATR-FTIR analysis. Spectra were normalized to the 1035 cm^{-1} peak, which can be attributed to C-O stretching vibrations. Since gelatin and HA-Tyr bear similar functional groups (amide, hydroxy, functional groups in tyramine moieties) spectra do now show obvious distinctive features of one component or the other. A notable trend was detectable at 860 cm^{-1} (**Figure 5**), where at the lowest degree of crosslinking (**Figure 5a**), the formation of a peak at day 1 was seen, with further increase at day 3, when a plateau was reached. In the medium crosslinked hydrogels (**Figure 5b**), changes were only observed starting at day 3. No obvious increases in the 860 cm^{-1} peak were observed at the highest degree of crosslinking or in the absence of gelatin (**Figure 5c-d**). The peak at 860 cm^{-1} may be attributed to aromatic compounds, such as tyramine and tyrosine, both present in our samples. An increase at 860 cm^{-1} associated with a decrease in other characteristic wavelengths (e.g., 3200-3400 cm^{-1}) may indicate gradual degradation or rearrangement of the polymers. Given that this increase was not observed in the absence of gelatin, we attributed this change to the gradual degradation of gelatin and subsequent exposure of the tyramine grafted on the hyaluronic acid.

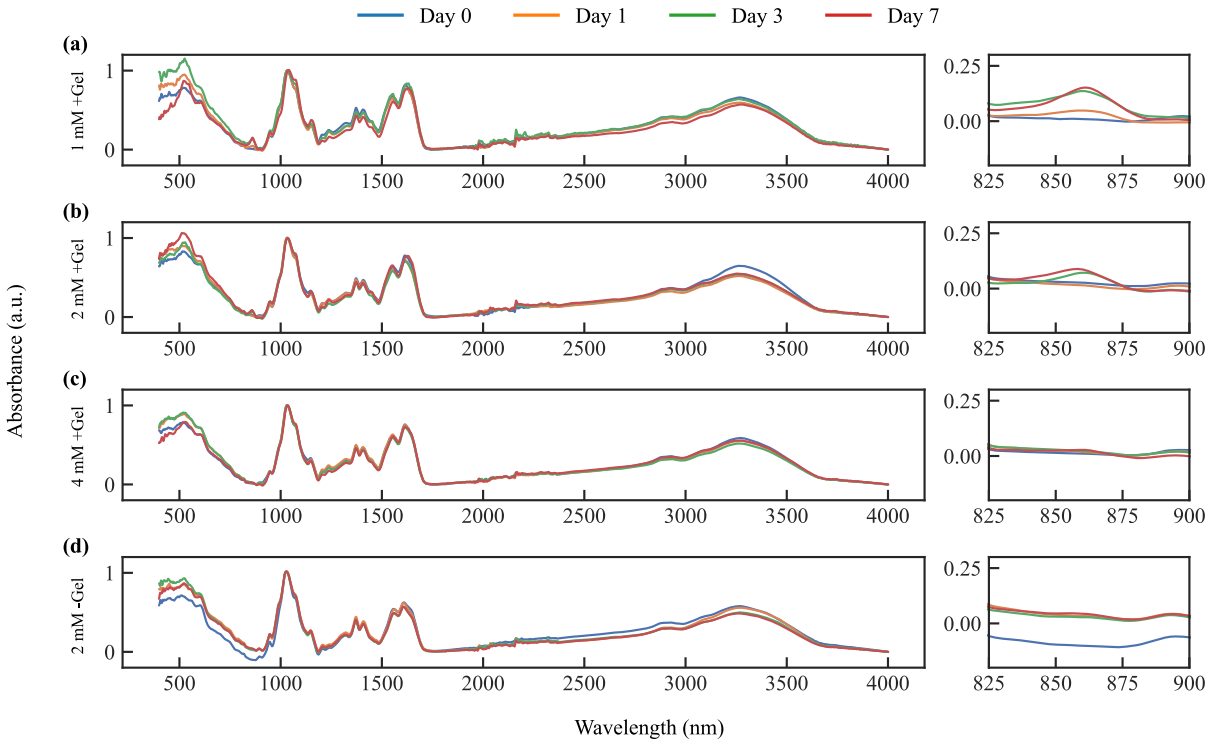

Figure 5. ATR-FTIR absorbance spectra of HA-Tyr/gelatin microgel samples prepared at different degrees of crosslinking. Panels on the right match the spectra on the left, zoomed in to the 825-900 cm^{-1} region. Presented as means of three technical replicates. (a) When samples are weakly crosslinked, an increase of the peak at 860 cm^{-1} corresponding to the length of incubation at 37 °C is observed. (b) The changes are less pronounced when the degree of crosslinking is increased, and only observed after 3 days of incubation. (c) No clear changes are observed in the strongly crosslinked samples. (d) Furthermore, there is no 860 cm^{-1} peak formation in the absence of gelatin.

3.5. *Printability*

We evaluated the bioink printability using a series of extrusion patterns. Straight extruded filaments were uniform with a mean diameter of 445 μm (SD = 25 μm). Filaments extruded 1 mm apart demonstrated a fused segment length of 0.9 mm (SD = 0.1 mm, **Figure 6a**). In producing grid structures, a printability index of 0.91 (SD = 0.02, **Figure 6b**) was achieved, indicating only a slight rounding of the square macropores. All gaps were bridged successfully in the pillar array test, with no sagging observed at 2 and 4 mm, and a 2.6° (SD = 0.4°, **Figure 6c**) deflection angle at 8 mm. Cylinders with a height of 7.5 mm and a single layer wall thickness were readily produced (**Figure 6d**).

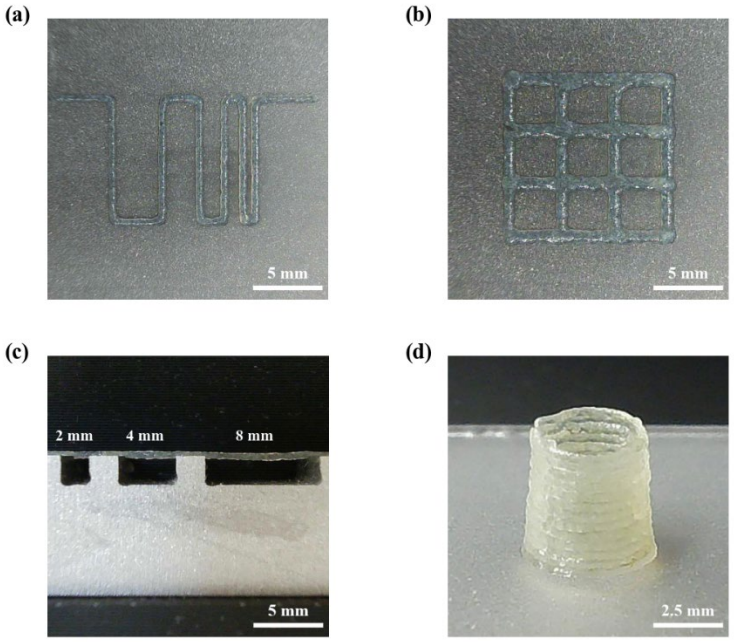

Figure 6. Representative samples of the bioink printability tests. (a) A spacing of slightly more than double the nozzle diameter (22G, 1 mm) is achieved without fusion, with good filament uniformity. (b) Square macropores are maintained in grid-like structures, with only minor rounding where perpendicular filaments meet. (c) The filament bridges gaps of up to 8 mm with minimal sagging. (d) Multi-layered constructs can be readily achieved. Depicted is a hollow cylinder approximately 7.5 mm tall.

3.6. *Cell viability*

The viability of nucleus pulposus cells embedded in hydrogels was assessed throughout 28 days of culture using confocal fluorescent microscopy. On the day of printing, cells maintained excellent viability in all three hydrogel stiffness compositions, exhibiting a round morphology (**Figure 7**, Day 0). During the first week of culture, cells in the softer hydrogels formulated with 1 mM and 2 mM SPS began to proliferate and exhibited spherical clustering, corresponding to the shape and size of gelatin microgels (**Figure 7**, Day 7). Cells in the stiff (4 mM SPS) formulation remained similarly distributed as after printing and did not exhibit such clustering, instead only showing minor spreading compared to earlier timepoints. By the end of the 28-day culture period, all three formulations exhibited higher cell densities indicative of proliferation. In softer hydrogels (1 and 2 mM SPS), large cell clusters formed, exhibiting an elongated morphology (**Figure 7**, Day 28). Cells in the stiffer hydrogel (4 mM SPS) demonstrated spherical clustering similar to the softer gels after the first week of culture. The cells remained viable throughout the entire culture period across all formulations.

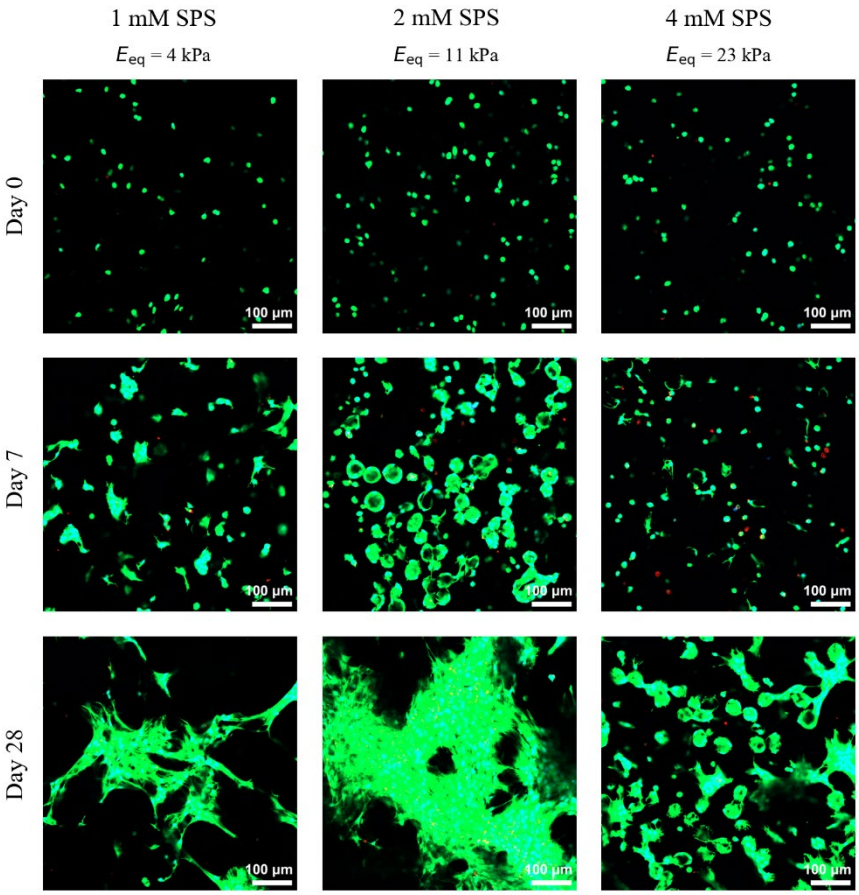

Figure 7. Confocal fluorescent characterization of nucleus pulposus cell viability in hydrogel-embedded cultures. Presented as representative slices out of 200 µm imaged stacks. Live cell cytoplasm was stained with calcein-AM (green), dead cell nuclei were stained with ethidium homodimer-1 (red), and all cell nuclei were stained with Hoechst 33342 (blue) to facilitate the identification of individual cells at high cell densities. Excellent cell viability was observed in the hydrogels on the day of printing and maintained up to 28 days of culture, with cell proliferation evident in all formulations. In softer hydrogels crosslinked with 1 and 2 mM of SPS, early clustering of cells in spherical structures resembling gelatin microgels was observed, suggesting infiltration of the hydrogel's porous structure. These structures were later replaced by larger clusters of elongated cells. The stiffer hydrogels crosslinked with 4 mM SPS exhibited a delay in cell clustering; however, these clusters were maintained by day 28 of culture. Scale bars represent a length of 100 µm.

3.7. Metabolic activity

The metabolic activity of encapsulated nucleus pulposus cells was quantified throughout 28 days of culture using the resazurin-based assay CellTiter-Blue. The measured values are consistent with fluorescent microscopy observations, showing that metabolic activity gradually increased over the 28 days in all formulations ($p < 0.001$, **Figure 8**). Despite starting with the same cell densities, the activity in softer hydrogels (1 and 2 mM SPS) was nearly double that observed in the stiffer hydrogels (4 mM SPS), with a statistically significant difference in metabolic activity across concentrations ($p = 0.048$). Notably, there was a considerable increase in metabolic activity between days 3 and 7 of culture across all formulations, although a pairwise statistical comparison of groups was not performed.

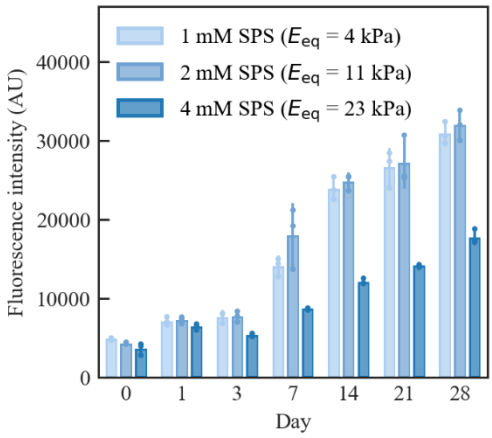

Figure 8. Quantification of the metabolic activity during 28 days of culture of nucleus pulposus cells embedded in hydrogels. Presented as means of three biological and two technical replicates each, with error bars indicating the standard deviation. The CellTiter-Blue assay demonstrated an increase in metabolic activity throughout the culture period for all formulations ($p < 0.001$). Differences in metabolic activity across concentrations were statistically significant ($p = 0.048$), with the softer hydrogels (1 and 2 mM SPS) exhibiting nearly double the activity of the stiffer hydrogel (4 mM SPS).

3.8. Matrix production

Composites with encapsulated bovine NP cells were evaluated for their capacity to support new matrix production. Safranin-O staining of glycosaminoglycans was strong on day 0 due to the high concentration of hyaluronic acid in the samples (**Figure 9**). A microporous HA-Tyr network with gelatin microgels (**Figure 9A**) and collagen fragments (**Figure 9B**) embedded was visible at all three compositions (1 mM, 2 mM, and 4 mM SPS), with no obvious differences dependent on the degree of crosslinking. At day 28, staining intensity varied considerably between groups. The least crosslinked samples exhibited a weak matrix with poor Safranin-O staining. An improved matrix integrity was observed in the 2 mM SPS group, though with no conclusive evidence of new matrix production. The strongly crosslinked group (4 mM SPS) exhibited a biphasic matrix. Large regions of dense matrix were visible in the samples (**Figure 9C**), separated by regions resembling the hyaluronic acid network on day 0 (**Figure 9D**). Presence of gelatin microgels could not be clearly established in any of the groups by day 28.

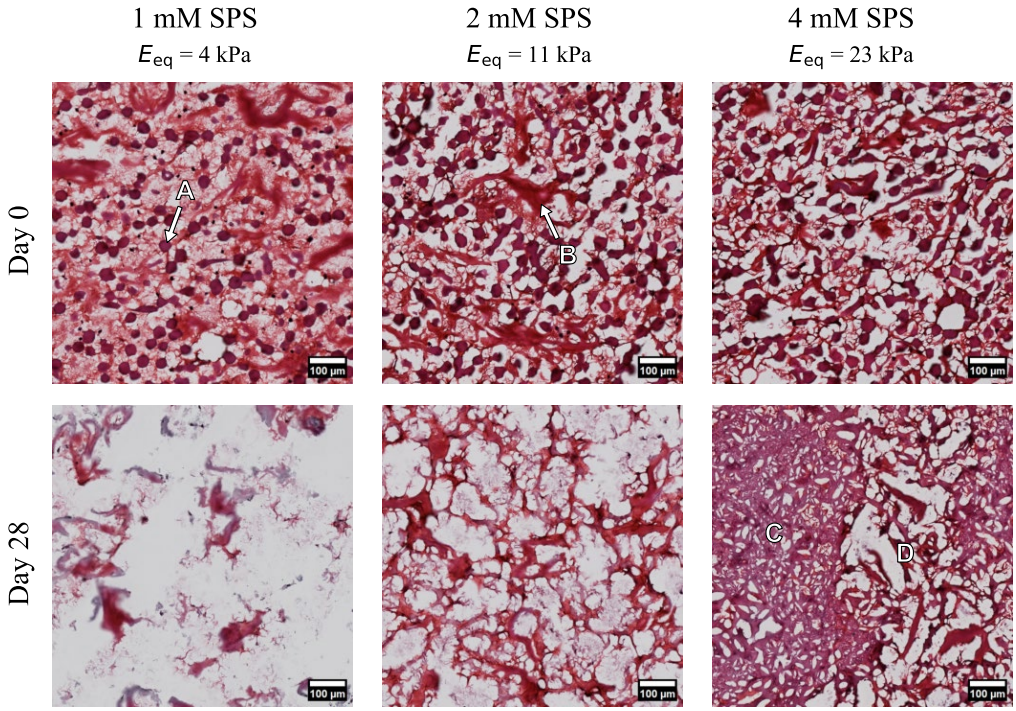

Figure 9. Representative images of NP cell-laden hydrogels stained with Safranin-O at days 0 and 28 of culture. Embedded gelatin microgels (A) and collagen fragments (B) are clearly visible at day 0 in all three compositions (1, 2, and 4 mM SPS). At day 28, the softer hydrogels exhibited a weak matrix with little or no new matrix production. In contrast, the stiffest hydrogels exhibited dense regions of nascent matrix (C) dispersed throughout the well-preserved hyaluronic acid structure (D).

3.9. Gene expression

The expression of nucleus pulposus markers was quantified using RT-qPCR (**Figure 10**). The selection of markers was based on their potential to differentiate between the nucleus pulposus, annulus fibrosus, and articular cartilage (Lv et al., 2014). Common anabolic markers such as COL1A2, COL2A1, and ACAN were selected due to the compositional differences of collagen type I and II, and aggrecan in the three tissue matrices. FOXF1 was selected due to its strong expression in the nucleus pulposus compared to the annulus fibrosus. SOX9 was similarly selected as a standard chondrogenic marker, and CDH2 as specifically a clear marker of healthy nucleus pulposus.

COL1A2 was upregulated significantly in the softest hydrogels and only slightly in the stiffer hydrogels, where it peaked at day 21 of culture. In contrast, COL2A1 was slightly downregulated in all three formulations. ACAN was somewhat upregulated in all formulations: in the 1 mM and 2 mM SPS formulations, the expression was transient with a peak at day 3, whereas the expression in the stiffer 4 mM peaked at day 21 and was sustained throughout the entire culture period.

Both FOXF1 and SOX9 remained consistent throughout 28 days of culture and did not appear to be affected by variations in material stiffness, whereas CDH2 was upregulated in all three formulations in the early days of culture and then decreased in the softer hydrogels (1 mM and 2 mM SPS). High levels of CDH2 expression were measured in the stiffer hydrogels (4 mM SPS) throughout all 28 days of culture.

Significant differences in expression over time were observed for all genes ($p < 0.016$), whereas the differences across concentrations were significant only for COL1A2 ($p = 0.002$), FOXF1 ($p < 0.001$), SOX9 ($p < 0.001$), and CDH2 ($p < 0.001$).

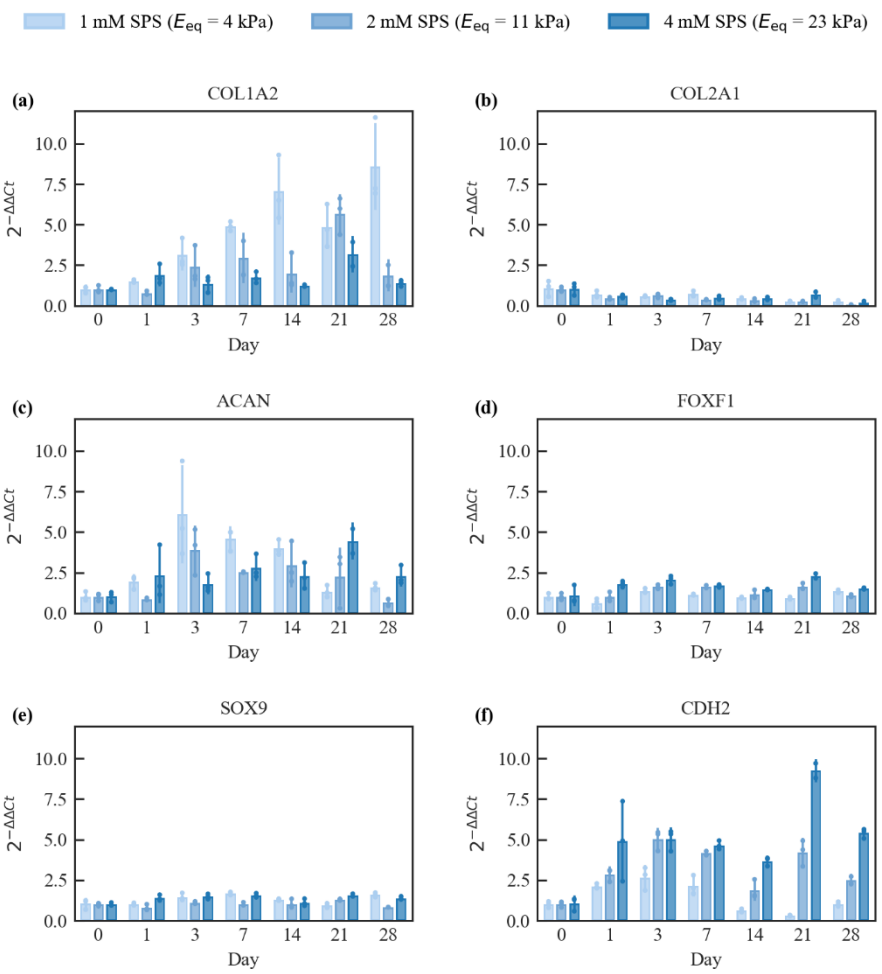

Figure 10. Expression of standard nucleus pulposus and chondrogenic markers by cells cultured for 28 days in hydrogels with varying stiffnesses. Presented as means of three biological replicates and two technical replicates each, with error bars indicating the standard deviation. A notable upregulation of COL1A2 in softer hydrogels (1 mM SPS) and CDH2 in stiffer hydrogels (4 mM SPS) was observed. FOXF1 and SOX9 remained relatively consistent throughout the 28-day culture period. COL2A1 exhibited a slight downward trend in expression by day 28. ACAN expression peaked in all three formulations by day 3 and decreased again by day 28 of the culture period. Significant differences in expression over time were observed for all genes ($p < 0.016$), whereas the differences across concentrations were significant only for COL1A2 ($p = 0.002$), FOXF1 ($p < 0.001$), SOX9 ($p < 0.001$), and CDH2 ($p < 0.001$).

3.10. Swelling and degradation

Samples were observed macroscopically throughout 28 days of culture, both with and without embedded cells. The initial swelling increased mass, as observed in all formulations after one day in culture (**Figure 11**). As expected, the swelling was inversely proportional to the degree of crosslinking ($p < 0.001$), with the softest hydrogels (1 mM SPS) swelling to almost 300% of their initial mass and volume, and the stiffer hydrogels (4 mM SPS) only to approximately 150%. No significant differences between hydrogels with and without embedded bovine NP cells or between time points within the 28-day culture period could be observed. All formulations remained stable in mass and volume after the first day of culture.

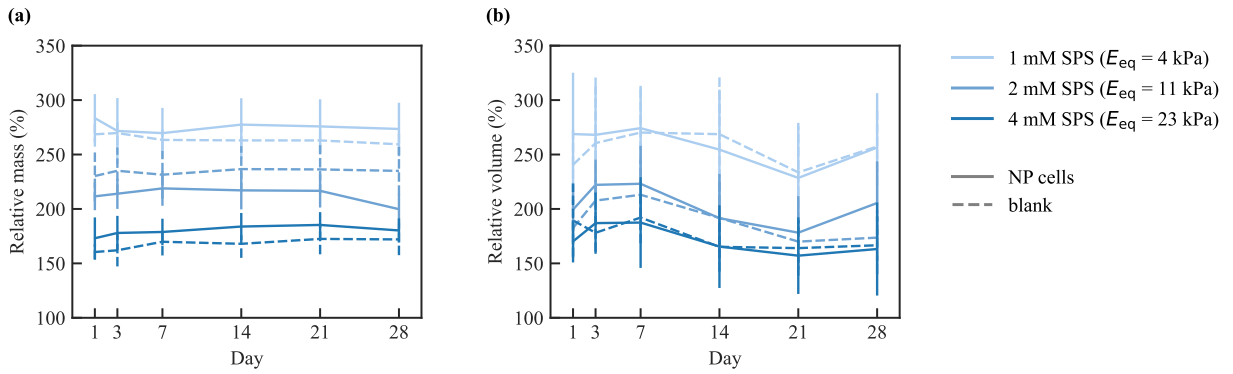

Figure 11. Relative mass (a) and volume (b) in hydrogels of various stiffnesses, with and without cells, were measured over a culture period of 28 days. Presented as means of three biological replicates, with error bars indicating the standard deviation. Rapid swelling, inversely proportional to the degree of crosslinking ($p < 0.001$), was observed in all formulations after a day of culture. No statistically significant differences were observed between hydrogels with or without cells, or across time points. All hydrogels remained stable after the initial swelling for the entire 28-day culture period.

4. Discussion

Advancements in our understanding of IVD degeneration hinge on our ability to faithfully replicate the disc's structure and function. Our study focused on the NP, which is crucial for maintaining the disc's hydration and mechanical resilience and is a key failure point during degeneration. We aimed to develop a composite hydrogel bioink that more accurately mimics the in vitro NP environment, offering broader relevance as a model for studying disc degeneration.

We formulated our bioink using a combination of native disc components, HA and collagen. Although previous studies have explored these components individually, few have combined them to leverage their individual advantages (Gloria et al., 2020). Using tyraminated HA enables the formation of tunable hydrogel networks with high swelling potential and varied mechanical properties. In combination with collagen, it provides essential biochemical cues, such as those experienced by cells in tissue (Guerrero et al., 2021). Our composite bioink further differentiates itself with biopolymer concentrations approximating physiological levels in human NP (3% HA and 2% collagen) (Singh et al., 2009). Such concentrations can present challenges when scaling up to physiological disc size in the centimeter range (G. D. O'Connell et al., 2007). A further challenge of high polymer concentrations involves preparing stable formulations of HA and collagen, which may form polyionic complexes, as has been discussed in previous literature (De Oliveira et al., 2023). In this initial study, we investigated isotropic cylindrical structures of 5 x 1.3 mm as a model to elucidate the effects of the viscoelastic properties on printability and cell response. It is important to note that, although NP is avascular, physiological nutrient diffusion may differ due to the size differences (C. Daly et al., 2016). In future models of the disc, these differences could be minimized through tuning of macro- and micro-porosity, which our material facilitates through its printability and gelatin component. To achieve a homogeneous composition at these high concentrations, we embedded pre-gelled collagen fragments within a bulk HA network. Although the use of mechanically fragmented hydrogels in injectable and extrudable formulations is well established (A. C. Daly, 2023; Muir et al., 2023), to our knowledge, this is the first time it has been utilized to ensure homogeneous distribution of a collagen fibrillar network throughout a bulk HA construct. An important consideration here is our use of type I collagen, rather than the type II present in native tissue. Both are fibril-forming collagens with similar biochemical properties. The choice of type I was driven primarily by

its availability and possibility of achieving relatively high concentrations. Although literature differs somewhat with respect to potential downsides of this substitution, it suggests that type I should nonetheless support discogenic differentiation (Chen et al., 2005; Rutgers et al., 2013). The bioink introduced in this study is not meant for tissue replacement.

Designing our hydrogels such that they could be fabricated using accessible and versatile approaches such as extrusion bioprinting, enables future integration in larger tissue-like constructs. Several studies have fabricated annulus fibrosus-like structures using techniques such as 3D printing, electrospinning, or melt electrowriting (Bhunia et al., 2021; Liu et al., 2022; Marshall et al., 2021; Nerurkar et al., 2007). Using multi-material or multimodal fabrication approaches, our bioink could be readily combined with such fibrous structures to form full IVD constructs. We facilitate this through the incorporation of sacrificial gelatin microgels, which modulate the rheological properties of our bioink and enable its extrusion under mild cell-compatible conditions, with pressures within a range that is not expected to impact cell viability (Nair et al., 2009). Additionally, microgel-based materials have actually been shown to shield cells from stresses during extrusion (Sinclair et al., 2018). In contrast to enzymatic crosslinking, where high cell densities can disrupt the gelation process (Petta et al., 2018), we found that sacrificial microgels robustly maintain viscoelasticity even with encapsulated cells. Previous literature has reported that such microgels are dissolvable under standard cell culture conditions and can enhance the rheological properties in a variety of bulk hydrogels, independent of the post-printing crosslinking parameters (Ouyang et al., 2022; Soliman et al., 2023). Our findings agree with this, having observed considerable rheological improvements upon incorporation of the microgels, as well as signs of gradual degradation, indicated by time- and crosslinking-dependent changes in sample FTIR spectra. Due to the presence of tyrosine in the gelatin structure, the precursor to tyramine, we expect our microgels to crosslink proportionally to the bulk gel, thereby reducing their degradation rate. Similar systems in previous work have delayed gelatin degradation by up to two weeks at high degrees of crosslinking, well in excess of concentrations used here (Soliman et al., 2023).

We demonstrated the versatility of our bottom-up, in vitro engineered model by showcasing the tunable properties of our material. Functionalizing HA with tyramine facilitates crosslinking through exposure to blue light. Through shear and compression mechanical tests, we have established that minor variations in crosslinker concentration (1-4 mM of SPS) enable us to achieve stiffness values ranging from approximately 5 to 20 kPa. The disc's stiffness increases drastically with compositional changes, particularly its hydration level. The stiffness of a healthy human NP starts at approximately 5 kPa in both compression and shear, and can increase up to tenfold in the most extreme cases of degeneration (Cloyd et al., 2007; Iatridis et al., 1997). This study covered a crucial subset of this range, from healthy to moderately degenerated discs, enabling us to mimic the mechanical changes associated with tissue degradation. As we have not exhaustively explored the limits of the photocrosslinking system in our composite, it may very well be applicable to a broader range of IVD states, including further increases in stiffness for the modelling of severely degenerated NP. Furthermore, changes in crosslinking density also modulate swelling behavior: the stiffer hydrogels exhibit proportionally less swelling. Free swelling of the native nucleus pulposus when removed from the annulus fibrosus can range from 200% in healthy to 60% in degenerated discs (Charnley, 1952; Iatridis et al., 1997). All our formulations maintain considerable swelling capabilities, with mass increases of 150-300% due to swelling observed. This high degree of hydration, attributable to the high HA content, is crucial in replicating the healthy NP mechanics as it supports the tissue's mechanical resilience (Iatridis et al., 1996). In order to explore degenerated NP states further, adaptations such as higher degrees of crosslinking, changes in polymer molecular weight and degree of functionalization, and addition of hydrophobic components might enable additional tunability of the swelling behavior. Future research should also investigate the behavior of this composite under confined conditions, including an annulus fibrosus ring, which limits swelling of the NP in its

physiological state. In addition to its flexibility, our crosslinking approach is rapid and has shown no adverse effects on encapsulated cells, with all compositions demonstrating excellent cell viability combined with an apparent cell proliferation. The cell compatibility may be attributed to the use of non-damaging blue visible light, in contrast to commonly employed crosslinking processes with ultraviolet light (Bryant et al., 2000).

Our observations of cell morphology and gene expression have shed light on how stiffness influences NP cells. Contrary to our initial hypothesis, the stiffest hydrogels - designed to mimic a degenerated disc – emerged as the most promising environment for NP cell culture. Within these stiffer matrices, cells preserved their rounded phenotype, mirroring native tissue characteristics (Risbud et al., 2015). They displayed a modest increase in aggrecan expression over the four-week culture while maintaining a low collagen I expression. In contrast, cells cultured in the softer formulations underwent considerable elongation, which correlated with increased collagen type I expression and decreased aggrecan expression after a brief initial increase on day 3, suggesting a shift toward a more pathological fibrotic phenotype. Notably, matrix stiffness also influenced the expression of the NP-specific marker CDH2, with upregulation observed in stiffer matrices corresponding with the native cell morphology and phenotype. These alterations may stem from the restricted cell mobility and matrix remodeling capabilities in stiffer hydrogels, which correspond to a denser polymer network (Ehrbar et al., 2011). Previous work has reported the importance of CHD2 expression in NP phenotype preservation: in degenerate human NP cells, which were CDH2 negative, cell clustering promoted re-expression of CDH2 and healthy matrix synthesis (Hwang et al., 2016). It is possible that the combination of a denser polymer network, which limits cell migration, and the presence of distributed spherical pores due to the use of sacrificial gelatin microgels, have together contributed to the preferential clustering of encapsulated cells and formation of CDH2-positive cell clusters. This was in agreement with our qualitative analysis of the sample matrix, where soft hydrogels exhibited a weak matrix by day 28 of culture and no sign of nascent matrix deposition, in contrast to the well-preserved structures and regions of nascent glycosaminoglycans in the stiffest hydrogels. Importantly, these modifications were obtained without supplementation of growth factors such as TGF-β and GDF-5, which could have masked the effects of the material. They are, therefore, inherent to the hydrogel's biochemical composition and mechanical properties. It is not clear if the absence of supplementation with ascorbic acid, an essential cofactor in the collagen synthesis process (Stone & Meister, 1962), is also responsible for the collagen type II downregulation or whether the observed gene expression profile is the result of a monolayer expansion, as observed with phenotypically similar cartilage chondrocytes (Tekari et al., 2014) (Okoro et al., 2023). The cells used in this study were used at passage 2, and nucleus pulposus cells may have the capacity to recover their original potential when transferred in a 3D environment (Gan et al., 2003). However, further work will be required to identify the optimal cell source and handling procedure for use with the developed biomaterials. Although our study focused on juvenile bovine NP cells, which were selected in order to validate the material's capacity to preserve the NP phenotype, the method could be adapted by using differentiating mesenchymal stromal cells (MSCs) into NP cells within HA/collagen hydrogels (Okoro et al., 2023), or induced-pluripotent stem cells. In the future, our composite system could therefore be expanded to MSCs or annulus fibrosus cells to broaden the relevance and applicability of our findings. Further investigating the stiffness-dependent behavior of these cells could offer more detailed insights into cell-specific responses, potentially expanding our bioink's clinical relevance beyond modelling to applications in regenerative medicine.

5. Conclusions

We introduce a composite bioink tailored for the biofabrication of NP constructs, formulated with 3% HA and 2% collagen, to approximate the composition of native NP tissue. By varying the degree of crosslinking, we achieved a wide range of swelling behaviors, compressive moduli, and shear moduli, encompassing both healthy and degenerated human IVD. Our bioink formulations demonstrate potential in supporting the NP phenotype without supplementation with growth factors. Furthermore, the varying crosslinking degrees enabled us to modulate cell morphologies, nascent matrix production, and gene expression profiles. Interestingly and somewhat paradoxically, softer substrates allowed increased cell spreading, with a tendency to de-differentiate into a fibroblast-like phenotype, whereas in stiffer substrates, cells maintained a rounder morphology, which better corresponds to NP. These observations were possible thanks to the absence of growth factors, providing valuable insight on how material cues influence biological properties, which could inform future model design and IVD research. This work expands the range of bioinks with high biopolymer concentrations available for the biofabrication of IVD-like constructs.

6. CRediT authorship contribution statement

GM: Conceptualization, data curation, formal analysis, investigation, methodology, project administration, validation, visualization, writing - original draft, writing – review & editing; SDO: investigation, methodology; MS: investigation, methodology; CLV: funding acquisition, methodology, project administration, resources, supervision, writing – review & editing; CH: funding acquisition, methodology, project administration, resources, supervision, writing – review & editing; SJF: funding acquisition, methodology, project administration, resources, supervision, writing – review & editing; MD: conceptualization, data curation, funding acquisition, methodology, project administration, resources, supervision, writing – review & editing.

7. Declaration of competing interest

The authors declare no conflict of interest.

8. Acknowledgements

This work was supported by the Swiss National Science Foundation and the French National Research Agency as bi-lateral project "INDEED", SNSF grant number 189310 and ANR grant number ANR-19-CE06-0028. Authors are grateful to Nicolas Devantay for technical assistance with sample preparation, rheology, and FTIR measurements.

9. Data availability

Data supporting this study's findings are available from the authors upon reasonable request.

10. References

Alini, M., Eisenstein, S. M., Ito, K., Little, C., Kettler, A. A., Masuda, K., Melrose, J., Ralphs, J., Stokes, I., & Wilke, H. J. (2008). Are animal models useful for studying human disc disorders/degeneration? *European Spine Journal*, *17*(1), 2–19. https://doi.org/10.1007/s00586-007-0414-y

Bhunia, B. K., Dey, S., Bandyopadhyay, A., & Mandal, B. B. (2021). 3D printing of annulus fibrosus anatomical equivalents recapitulating angle-ply architecture for intervertebral disc replacement. *Applied Materials Today*, *23*, 101031. https://doi.org/10.1016/j.apmt.2021.101031

Bryant, S. J., Nuttelman, C. R., & Anseth, K. S. (2000). Cytocompatibility of UV and visible light photoinitiating systems on cultured NIH/3T3 fibroblasts in vitro. *Journal of Biomaterials Science, Polymer Edition*, *11*(5), 439–457. https://doi.org/10.1163/156856200743805

Charnley, J. (1952). The Imbibition of Fluid as a Cause of Herniation of the Nucleus Pulposus. *Originally Published as Volume 1, Issue 6699*, *259*(6699), 124–127. https://doi.org/10.1016/S0140-6736(52)92428-8

Chen, C. W., Tsai, Y. H., Deng, W. P., Shih, S. N., Fang, C. L., Burch, J. G., Chen, W. H., & Lai, W. F. (2005). Type I and II collagen regulation of chondrogenic differentiation by mesenchymal progenitor cells. *Journal of Orthopaedic Research*, *23*(2), 446–453. https://doi.org/10.1016/j.orthres.2004.09.002

Cloyd, J. M., Malhotra, N. R., Weng, L., Chen, W., Mauck, R. L., & Elliott, D. M. (2007). Material properties in unconfined compression of human nucleus pulposus, injectable hyaluronic acid-based hydrogels and tissue engineering scaffolds. *European Spine Journal*, *16*(11), 1892–1898. https://doi.org/10.1007/s00586-007-0443-6

Daly, A. C. (2023). Granular Hydrogels in Biofabrication: Recent Advances and Future Perspectives. *Advanced Healthcare Materials*, *n/a*(n/a), 2301388. https://doi.org/10.1002/adhm.202301388

Daly, C., Ghosh, P., Jenkin, G., Oehme, D., & Goldschlager, T. (2016). A Review of Animal Models of Intervertebral Disc Degeneration: Pathophysiology, Regeneration, and Translation to the Clinic. *BioMed Research International*, *2016*(1), 5952165. https://doi.org/10.1155/2016/5952165

Darr, A., & Calabro, A. (2009). Synthesis and characterization of tyramine-based hyaluronan hydrogels. *Journal of Materials Science: Materials in Medicine*, *20*(1), 33–44. https://doi.org/10.1007/s10856-008-3540-0

De Oliveira, S., Miklosic, G., Veziers, J., Grastilleur, S., Coradin, T., Le Visage, C., Guicheux, J., D'Este, M., & Hélary, C. (2023). Optimizing the physical properties of collagen/hyaluronan hydrogels by inhibition of polyionic complexes formation at pH close to the collagen isoelectric point. *Soft Matter*, *19*(46), 9027–9035. https://doi.org/10.1039/D3SM01330H

DePalma, M. J., Ketchum, J. M., & Saullo, T. (2011). What Is the Source of Chronic Low Back Pain and Does Age Play a Role? *Pain Medicine*, *12*(2), 224–233. https://doi.org/10.1111/j.1526-4637.2010.01045.x

Ehrbar, M., Sala, A., Lienemann, P., Ranga, A., Mosiewicz, K., Bittermann, A., Rizzi, S. C., Weber, F. E., & Lutolf, M. P. (2011). Elucidating the Role of Matrix Stiffness in 3D Cell Migration and Remodeling. *Biophysical Journal*, *100*(2), 284–293. https://doi.org/10.1016/j.bpj.2010.11.082

Erwin, W. M., Ashman, K., O'Donnel, P., & Inman, R. D. (2006). Nucleus pulposus notochord cells secrete connective tissue growth factor and Up-regulate proteoglycan expression by intervertebral disc chondrocytes. *Arthritis & Rheumatism*, *54*(12), 3859–3867. https://doi.org/10.1002/art.22258

Freemont, A., Peacock, T., Goupille, P., Hoyland, J., O'Brien, J., & Jayson, M. (1997). Nerve ingrowth into diseased intervertebral disc in chronic back pain. *The Lancet*, *350*(9072), 178–181. https://doi.org/10.1016/S0140-6736(97)02135-1

Gan, J. C., Ducheyne, P., Vresilovic, E. J., & Shapiro, I. M. (2003). Intervertebral Disc Tissue Engineering II: Cultures of Nucleus Pulposus Cells. *Clinical Orthopaedics and Related Research®*, *411*, 315. https://doi.org/10.1097/01.blo.0000063797.98363.d3

Gawri, R., Moir, J., Ouellet, J., Beckman, L., Steffen, T., Roughley, P., & Haglund, L. (2014). Physiological Loading Can Restore the Proteoglycan Content in a Model of Early IVD Degeneration. *PLOS ONE*, *9*(7), e101233. https://doi.org/10.1371/journal.pone.0101233

Gloria, A., Russo, T., D'Amora, U., Santin, M., De Santis, R., & Ambrosio, L. (2020). Customised multiphasic nucleus/annulus scaffold for intervertebral disc repair/regeneration. *Connective Tissue Research*, *61*(2), 152–162. https://doi.org/10.1080/03008207.2019.1650037

Guerrero, J., Häckel, S., Croft, A., Hoppe, S., Albers, C., & Gantenbein, B. (2021). The nucleus pulposus microenvironment in the intervertebral disc: The fountain of youth? *European Cells and Materials*, *41*, 707–738. https://doi.org/10.22203/eCM.v041a46

Gullbrand, S. E., Ashinsky, B. G., Bonnevie, E. D., Kim, D. H., Engiles, J. B., Smith, L. J., Elliott, D. M., Schaer, T. P., Smith, H. E., & Mauck, R. L. (2018). Long-term mechanical function and integration of an implanted tissue-engineered intervertebral disc. *Science Translational Medicine*, *10*(468). https://doi.org/10.1126/scitranslmed.aau0670

Hartvigsen, J., Hancock, M. J., Kongsted, A., Louw, Q., Ferreira, M. L., Genevay, S., Hoy, D., Karppinen, J., Pransky, G., Sieper, J., Smeets, R. J., Underwood, M., Buchbinder, R., Hartvigsen, J., Cherkin, D., Foster, N. E., Maher, C. G., Underwood, M., van Tulder, M., … Woolf, A. (2018). What low back pain is and why we need to pay attention. *The Lancet*, *391*(10137), 2356–2367. https://doi.org/10.1016/S0140-6736(18)30480-X

Hinton, T. J., Jallerat, Q., Palchesko, R. N., Park, J. H., Grodzicki, M. S., Shue, H.-J., Ramadan, M. H., Hudson, A. R., & Feinberg, A. W. (2015). Three-dimensional printing of complex biological structures by freeform reversible embedding of suspended hydrogels. *Science Advances*, *1*(9), e1500758. https://doi.org/10.1126/sciadv.1500758

Hsieh, A. H., & Twomey, J. D. (2010). Cellular mechanobiology of the intervertebral disc: New directions and approaches. *Journal of Biomechanics*, *43*(1), 137–145. https://doi.org/10.1016/j.jbiomech.2009.09.019

Hwang, P. Y., Jing, L., Chen, J., Lim, F.-L., Tang, R., Choi, H., Cheung, K. M., Risbud, M. V., Gersbach, C. A., Guilak, F., Leung, V. Y., & Setton, L. A. (2016). N-cadherin is Key to Expression of the Nucleus Pulposus Cell Phenotype under Selective Substrate Culture Conditions. *Scientific Reports*, *6*(1), 28038. https://doi.org/10.1038/srep28038

Iatridis, J. C., Kumar, S., Foster, R. J., Weidenbaum, M., & Mow, V. C. (1999). Shear mechanical properties of human lumbar annulus fibrosus. *Journal of Orthopaedic Research*, *17*(5), 732–737. https://doi.org/10.1002/jor.1100170517

Iatridis, J. C., Setton, L. A., Weidenbaum, M., & Mow, V. C. (1997). Alterations in the mechanical behavior of the human lumbar nucleus pulposus with degeneration and aging. *Journal of Orthopaedic Research*, *15*(2), 318–322. https://doi.org/10.1002/jor.1100150224

Iatridis, J. C., Weidenbaum, M., Setton, L. A., & Mow, V. C. (1996). Is the Nucleus Pulposus a Solid or a Fluid? Mechanical Behaviors of the Nucleus Pulposus of the Human Intervertebral Disc. *Spine*, *21*(10), 1174–1184.

Lazaro-Pacheco, D., Mohseni, M., Rudd, S., Cooper-White, J., & Holsgrove, T. P. (2023). The role of biomechanical factors in models of intervertebral disc degeneration across multiple length scales. *APL Bioengineering*, *7*(2), 021501. https://doi.org/10.1063/5.0137698

Le Maitre, C. L., Freemont, A. J., & Hoyland, J. A. (2005). The role of interleukin-1 in the pathogenesis of human Intervertebral disc degeneration. *Arthritis Research & Therapy*, *7*(4), Article 4. https://doi.org/10.1186/ar1732

Le Maitre, C. L., Freemont, A. J., & Hoyland, J. A. (2007). Accelerated cellular senescence in degenerate intervertebral discs: A possible role in the pathogenesis of intervertebral disc degeneration. *Arthritis Research & Therapy*, *9*(3), Article 3. https://doi.org/10.1186/ar2198

Liu, Z., Wang, H., Yuan, Z., Wei, Q., Han, F., Chen, S., Xu, H., Li, J., Wang, J., Li, Z., Chen, Q., Fuh, J., Ding, L., Wang, H., & Li, B. (2022). High-resolution 3D printing of angle-ply annulus fibrosus

scaffolds for intervertebral disc regeneration. *Biofabrication*, *15*(1), 015015. https://doi.org/10.1088/1758-5090/aca71f

Lv, F., Leung, V. Y. L., Huang, S., Huang, Y., Sun, Y., & Cheung, K. M. C. (2014). In search of nucleus pulposus-specific molecular markers. *Rheumatology*, *53*(4), 600–610. https://doi.org/10.1093/rheumatology/ket303

Mainardi, A., Cambria, E., Occhetta, P., Martin, I., Barbero, A., Schären, S., Mehrkens, A., & Krupkova, O. (2022). Intervertebral Disc-on-a-Chip as Advanced In Vitro Model for Mechanobiology Research and Drug Testing: A Review and Perspective. *Frontiers in Bioengineering and Biotechnology*, *9*. https://doi.org/10.3389/fbioe.2021.826867

Marshall, S. L., Jacobsen, T. D., Emsbo, E., Murali, A., Anton, K., Liu, J. Z., Lu, H. H., & Chahine, N. O. (2021). Three-Dimensional-Printed Flexible Scaffolds Have Tunable Biomimetic Mechanical Properties for Intervertebral Disc Tissue Engineering. *ACS Biomaterials Science & Engineering*, *7*(12), 5836–5849. https://doi.org/10.1021/acsbiomaterials.1c01326

Martins, D. E., Medeiros, V. P. de, Wajchenberg, M., Paredes-Gamero, E. J., Lima, M., Reginato, R. D., Nader, H. B., Puertas, E. B., & Faloppa, F. (2018). Changes in human intervertebral disc biochemical composition and bony end plates between middle and old age. *PLOS ONE*, *13*(9), e0203932. https://doi.org/10.1371/journal.pone.0203932

Muir, V. G., Fainor, M., Orozco, B. S., Hilliard, R., Boyes, M., Smith, H. E., Mauck, R. L., Schaer, T., Burdick, J. A., & Gullbrand, S. E. (2023). Injectable Radiopaque Hyaluronic Acid Granular Hydrogels for Intervertebral Disc Repair. *Advanced Healthcare Materials*, *n/a*(n/a), 2303326. https://doi.org/10.1002/adhm.202303326

Nair, K., Gandhi, M., Khalil, S., Yan, K. C., Marcolongo, M., Barbee, K., & Sun, W. (2009). Characterization of cell viability during bioprinting processes. *Biotechnology Journal*, *4*(8), 1168–1177. https://doi.org/10.1002/biot.200900004

Nerurkar, N. L., Elliott, D. M., & Mauck, R. L. (2007). Mechanics of oriented electrospun nanofibrous scaffolds for annulus fibrosus tissue engineering. *Journal of Orthopaedic Research*, *25*(8), 1018–1028. https://doi.org/10.1002/jor.20384

Nikonenko, N. A., Buslov, D. K., Sushko, N. I., & Zhbankov, R. G. (2000). Investigation of stretching vibrations of glycosidic linkages in disaccharides and polysaccarides with use of IR spectra deconvolution. *Biopolymers*, *57*(4), 257–262. https://doi.org/10.1002/1097-0282(2000)57:4<257::AID-BIP7>3.0.CO;2-3

O'Connell, C., Ren, J., Pope, L., Zhang, Y., Mohandas, A., Blanchard, R., Duchi, S., & Onofrillo, C. (2020). Characterizing Bioinks for Extrusion Bioprinting: Printability and Rheology. In J. M. Crook (Ed.), *3D Bioprinting* (Vol. 2140, pp. 111–133). Springer US. https://doi.org/10.1007/978-1-0716-0520-2_7

O'Connell, G. D., Vresilovic, E. J., & Elliott, D. M. (2007). Comparison of Animals Used in Disc Research to Human Lumbar Disc Geometry. *Spine*, *32*(3), 328. https://doi.org/10.1097/01.brs.0000253961.40910.c1

Okoro, P. D., Frayssinet, A., Oliveira, S. D., Rouquier, L., Miklosic, G., D'Este, M., Potier, E., & Hélary, C. (2023). Combining biomimetic collagen/hyaluronan hydrogels with discogenic growth factors promotes mesenchymal stroma cell differentiation into Nucleus Pulposus like cells. *Biomaterials Science*, *11*(24), 7768–7783. https://doi.org/10.1039/D3BM01025B

Ouyang, L., Wojciechowski, J. P., Tang, J., Guo, Y., & Stevens, M. M. (2022). Tunable Microgel-Templated Porogel (MTP) Bioink for 3D Bioprinting Applications. *Advanced Healthcare Materials*, *11*(8), 2200027. https://doi.org/10.1002/adhm.202200027

Pachitariu, M., & Stringer, C. (2022). Cellpose 2.0: How to train your own model. *Nature Methods*, *19*(12), 1634–1641. https://doi.org/10.1038/s41592-022-01663-4

Pattappa, G., Li, Z., Peroglio, M., Wismer, N., Alini, M., & Grad, S. (2012). Diversity of intervertebral disc cells: Phenotype and function. *Journal of Anatomy*, *221*(6), 480–496. https://doi.org/10.1111/j.1469-7580.2012.01521.x

Paul, C. P. L., Zuiderbaan, H. A., Doulabi, B. Z., Veen, A. J. van der, Ven, P. M. van de, Smit, T. H., Helder, M. N., Royen, B. J. van, & Mullender, M. G. (2012). Simulated-Physiological Loading Conditions Preserve Biological and Mechanical Properties of Caprine Lumbar Intervertebral Discs in Ex Vivo Culture. *PLOS ONE*, *7*(3), e33147. https://doi.org/10.1371/journal.pone.0033147

Petta, D., Armiento, A. R., Grijpma, D., Alini, M., Eglin, D., & D'Este, M. (2018). 3D bioprinting of a hyaluronan bioink through enzymatic-and visible light-crosslinking. *Biofabrication*, *10*(4), 044104. https://doi.org/10.1088/1758-5090/aadf58

Phillips, K. L. E., Chiverton, N., Michael, A. L., Cole, A. A., Breakwell, L. M., Haddock, G., Bunning, R. A., Cross, A. K., & Le Maitre, C. L. (2013). The cytokine and chemokine expression profile of nucleus pulposus cells: Implications for degeneration and regeneration of the intervertebral disc. *Arthritis Research & Therapy*, *15*(6), Article 6. https://doi.org/10.1186/ar4408

Poletto, D. L., Crowley, J. D., Tanglay, O., Walsh, W. R., & Pelletier, M. H. (2023). Preclinical in vivo animal models of intervertebral disc degeneration. Part 1: A systematic review. *JOR SPINE*, *6*(1), e1234. https://doi.org/10.1002/jsp2.1234

Ribeiro, A., Blokzijl, M. M., Levato, R., Visser, C. W., Castilho, M., Hennink, W. E., Vermonden, T., & Malda, J. (2017). Assessing bioink shape fidelity to aid material development in 3D bioprinting. *Biofabrication*, *10*(1), 014102. https://doi.org/10.1088/1758-5090/aa90e2

Risbud, M. V., Schoepflin, Z. R., Mwale, F., Kandel, R. A., Grad, S., Iatridis, J. C., Sakai, D., & Hoyland, J. A. (2015). Defining the phenotype of young healthy nucleus pulposus cells: Recommendations of the Spine Research Interest Group at the 2014 annual ORS meeting. *Journal of Orthopaedic Research*, *33*(3), 283–293. https://doi.org/10.1002/jor.22789

Roberts, S., Urban, J. P. G., Evans, H., & Eisenstein, S. M. (1996). Transport Properties of the Human Cartilage Endplate in Relation to Its Composition and Calcification. *Spine*, *21*(4), 415.

Romaniyanto, Mahyudin, F., Sigit Prakoeswa, C. R., Notobroto, H. B., Tinduh, D., Ausrin, R., Rantam, F. A., Suroto, H., Utomo, D. N., & Rhatomy, S. (2022). An update of current therapeutic approach for Intervertebral Disc Degeneration: A review article. *Annals of Medicine and Surgery*, *77*, 103619. https://doi.org/10.1016/j.amsu.2022.103619

Rutgers, M., Saris, D. B., Vonk, L. A., van Rijen, M. H., Akrum, V., Langeveld, D., van Boxtel, A., Dhert, W. J., & Creemers, L. B. (2013). Effect of Collagen Type I or Type II on Chondrogenesis by Cultured Human Articular Chondrocytes. *Tissue Engineering Part A*, *19*(1–2), 59–65. https://doi.org/10.1089/ten.tea.2011.0416

Schmitz, T. C., Salzer, E., Crispim, J. F., Fabra, G. T., LeVisage, C., Pandit, A., Tryfonidou, M., Maitre, C. L., & Ito, K. (2020). Characterization of biomaterials intended for use in the nucleus pulposus of degenerated intervertebral discs. *Acta Biomaterialia*, *114*, 1–15. https://doi.org/10.1016/j.actbio.2020.08.001

Schwab, A., Levato, R., D'Este, M., Piluso, S., Eglin, D., & Malda, J. (2020). Printability and Shape Fidelity of Bioinks in 3D Bioprinting. *Chemical Reviews*. https://doi.org/10.1021/acs.chemrev.0c00084

Seabold, S., & Perktold, J. (2010). *Statsmodels: Econometric and Statistical Modeling with Python*. 92–96. https://doi.org/10.25080/Majora-92bf1922-011

Setton, L. A., & Chen, J. (2004). Cell Mechanics and Mechanobiology in the Intervertebral Disc. *Spine*, *29*(23), 2710. https://doi.org/10.1097/01.brs.0000146050.57722.2a

Shirazi-Adl, A., Taheri, M., & Urban, J. P. G. (2010). Analysis of cell viability in intervertebral disc: Effect of endplate permeability on cell population. *Journal of Biomechanics*, *43*(7), 1330–1336. https://doi.org/10.1016/j.jbiomech.2010.01.023

Sinclair, A., O'Kelly, M. B., Bai, T., Hung, H., Jain, P., & Jiang, S. (2018). Self-Healing Zwitterionic Microgels as a Versatile Platform for Malleable Cell Constructs and Injectable Therapies. *Advanced Materials*, *30*(39), 1803087. https://doi.org/10.1002/adma.201803087

Singh, K., Masuda, K., Thonar, E. J.-M. A., An, H. S., & Cs-Szabo, G. (2009). Age-Related Changes in the Extracellular Matrix of Nucleus Pulposus and Anulus Fibrosus of Human Intervertebral Disc. *Spine*, *34*(1), 10. https://doi.org/10.1097/BRS.0b013e31818e5ddd

Soliman, B. G., Longoni, A., Wang, M., Li, W., Bernal, P. N., Cianciosi, A., Lindberg, G. C. J., Malda, J., Groll, J., Jungst, T., Levato, R., Rnjak-Kovacina, J., Woodfield, T. B. F., Zhang, Y. S., & Lim, K. S. (2023). Programming Delayed Dissolution Into Sacrificial Bioinks For Dynamic Temporal Control of Architecture within 3D-Bioprinted Constructs. *Advanced Functional Materials*, *33*(8), 2210521. https://doi.org/10.1002/adfm.202210521

Stone, N., & Meister, A. (1962). Function of Ascorbic Acid in the Conversion of Proline to Collagen Hydroxyproline. *Nature*, *194*(4828), 555–557. https://doi.org/10.1038/194555a0

Sztrolovics, R., Alini, M., Roughley, P. J., & Mort, J. S. (1997). Aggrecan degradation in human intervertebral disc and articular cartilage. *Biochemical Journal*, *326*(1), 235–241. https://doi.org/10.1042/bj3260235

Tekari, A., Luginbuehl, R., Hofstetter, W., & Egli, R. J. (2014). Chondrocytes expressing intracellular collagen type II enter the cell cycle and co-express collagen type I in monolayer culture. *Journal of Orthopaedic Research*, *32*(11), 1503–1511. https://doi.org/10.1002/jor.22690

Vergroesen, P.-P. A., Kingma, I., Emanuel, K. S., Hoogendoorn, R. J. W., Welting, T. J., van Royen, B. J., van Dieën, J. H., & Smit, T. H. (2015). Mechanics and biology in intervertebral disc degeneration: A vicious circle. *Osteoarthritis and Cartilage*, *23*(7), 1057–1070. https://doi.org/10.1016/j.joca.2015.03.028

Vernengo, A. J., Grad, S., Eglin, D., Alini, M., & Li, Z. (2020). Bioprinting Tissue Analogues with Decellularized Extracellular Matrix Bioink for Regeneration and Tissue Models of Cartilage and Intervertebral Discs. *Advanced Functional Materials*, *30*(44), 1909044. https://doi.org/10.1002/adfm.201909044

Virtanen, P., Gommers, R., Oliphant, T. E., Haberland, M., Reddy, T., Cournapeau, D., Burovski, E., Peterson, P., Weckesser, W., Bright, J., van der Walt, S. J., Brett, M., Wilson, J., Millman, K. J., Mayorov, N., Nelson, A. R. J., Jones, E., Kern, R., Larson, E., … van Mulbregt, P. (2020). SciPy 1.0: Fundamental algorithms for scientific computing in Python. *Nature Methods*, *17*(3), 261–272. https://doi.org/10.1038/s41592-019-0686-2

Vos, T., Flaxman, A. D., Naghavi, M., Lozano, R., Michaud, C., Ezzati, M., Shibuya, K., Salomon, J. A., Abdalla, S., Aboyans, V., Abraham, J., Ackerman, I., Aggarwal, R., Ahn, S. Y., Ali, M. K., AlMazroa, M. A., Alvarado, M., Anderson, H. R., Anderson, L. M., … Murray, C. J. (2012). Years lived with disability (YLDs) for 1160 sequelae of 289 diseases and injuries 1990–2010: A systematic analysis for the Global Burden of Disease Study 2010. *The Lancet*, *380*(9859), 2163–2196. https://doi.org/10.1016/S0140-6736(12)61729-2

Wang, Y., Kang, J., Guo, X., Zhu, D., Liu, M., Yang, L., Zhang, G., & Kang, X. (2022). Intervertebral Disc Degeneration Models for Pathophysiology and Regenerative Therapy -Benefits and Limitations. *Journal of Investigative Surgery*, *35*(4), 935–952. https://doi.org/10.1080/08941939.2021.1953640

Wuertz, K., Godburn, K., MacLean, J. J., Barbir, A., Stinnett Donnelly, J., Roughley, P. J., Alini, M., & Iatridis, J. C. (2009). In vivo remodeling of intervertebral discs in response to short- and long-

term dynamic compression. *Journal of Orthopaedic Research*, *27*(9), 1235–1242. https://doi.org/10.1002/jor.20867

Yang, J., Wang, L., Zhang, W., Sun, Z., Li, Y., Yang, M., Zeng, D., Peng, B., Zheng, W., Jiang, X., & Yang, G. (2018). Reverse Reconstruction and Bioprinting of Bacterial Cellulose-Based Functional Total Intervertebral Disc for Therapeutic Implantation. *Small*, *14*(7), 1702582. https://doi.org/10.1002/smll.201702582

Zhao, C.-Q., Wang, L.-M., Jiang, L.-S., & Dai, L.-Y. (2007). The cell biology of intervertebral disc aging and degeneration. *Ageing Research Reviews*, *6*(3), 247–261. https://doi.org/10.1016/j.arr.2007.08.001